



# A geometric framework for ensemble average propagator reconstruction from diffusion MRI

Baba C. Vemuri<sup>a,\*</sup>, Jiaqi Sun<sup>a</sup>, Monami Banerjee<sup>a</sup>, Zhixin Pan<sup>a</sup>, Sara M. Turner<sup>b</sup>, David D. Fuller<sup>b</sup>, John R. Forder<sup>c</sup>, Alireza Entezari<sup>a</sup>

<sup>a</sup> Department of Computer Information Science and Engineering, University of Florida, Gainesville, FL 32611, USA

<sup>b</sup> Department of Physical Therapy, University of Florida, Gainesville, FL 32610, USA

<sup>c</sup> Department of Radiology, University of Florida, Gainesville, FL 32611, USA

## ARTICLE INFO

### Article history:

Received 6 August 2018

Revised 13 March 2019

Accepted 24 June 2019

Available online 2 July 2019

### Keywords:

Diffusion MRI

Ensemble average propagator

Dictionary learning

Sparse coding

Riemannian manifold

Rényi entropy

Imaging biomarker

## ABSTRACT

Diffusion-weighted magnetic resonance imaging (dMRI) is a non-invasive technique to probe the complex micro-architecture of the tissue being imaged. The diffusional properties of the tissue at the imaged resolution are well captured by the ensemble average propagator (EAP), which is a probability density function characterizing the probability of water molecule diffusion. Many properties in the form of imaging 'stains' can then be computed from the EAP that can serve as bio-markers for a variety of diseases. This motivates the development of methods for the accurate estimation of the EAPs from dMRI, which is an actively researched area in dMRI analysis. To this end, in the recent past, dictionary learning (DL) techniques have been applied by many researchers for accurate reconstruction of the EAP fields from dMRI scans of the central nervous system (CNS). However, most of the DL-based methods did not exploit the geometry of the space of the EAPs, which are probability density functions. By exploiting the geometry of the space of probability density functions, it is possible to reconstruct EAPs that satisfy the mathematical properties of a density function and hence yield better accuracy in the EAP field reconstruction.

Using a square root density parameterization, the EAPs can be mapped to a unit Hilbert sphere, which is a smooth manifold with well known geometry that we will exploit in our formulation of the DL problem. Thus, in this paper, we present a general formulation of the DL problem for data residing on smooth manifolds and in particular the manifold of EAPs, along with a numerical solution using an alternating minimization method. We then showcase the properties and the performance of our algorithm on the reconstruction of the EAP field in a patch-wise manner from the dMRI data. Through several synthetic, phantom and real data examples, we demonstrate that our non-linear DL-based approach produces accurate and spatially smooth estimates of the EAP field from dMRI in comparison to the state-of-the-art EAP reconstruction method called the MAPL method, as well as the linear DL-based EAP reconstruction approaches. To further demonstrate the accuracy and utility of our approach, we compute an entropic anisotropy measure (HA), that is a function of the well known Rényi entropy, from the EAP fields of control and injured rat spinal cords respectively. We demonstrate its utility as an imaging 'stain' via a quantitative comparison of HA maps computed from EAP fields estimated using our method and competing methods. The quantitative comparison is achieved using a two sample *t*-test and the results of significance are displayed for a visualization of regions of the spinal cord affected most by the injury.

© 2019 Elsevier B.V. All rights reserved.

## 1. Introduction

Diffusion weighted MRI (dMRI) is a non-invasive imaging technique which facilitates exploration of the complex micro-structure of fibrous tissues (such as white matter in the central neural system (CNS)) through sensing the diffusion of water molecules

(Basser et al., 1994). Water diffusion can be fully characterized by the diffusion probability density function (PDF) known as the ensemble average propagator (EAP) (Callaghan, 1991). Under the narrow pulse assumption, the ensemble average propagator denoted by  $P(\mathbf{r})$  is related to the attenuation of the diffusion sensitized signal  $E(\mathbf{q})$  through the Fourier transform relationship (Callaghan, 1991):

$$P(\mathbf{r}) = \int E(\mathbf{q}) \exp(-2\pi i \mathbf{q} \cdot \mathbf{r}) d\mathbf{q} \quad (1)$$

\* Corresponding author.

E-mail address: [vemuri@ufl.edu](mailto:vemuri@ufl.edu) (B.C. Vemuri).

where  $E(\mathbf{q}) = S(\mathbf{q})/S_0$  and  $S_0$  is the MR signal with zero diffusion gradient.

The information captured by the EAP about the water diffusion process makes its reconstruction one of the most important and actively researched problems in the field of diffusion MRI processing over the past decade. An accurate EAP reconstruction approach is critical and essential to other dMRI applications such as fiber tractography, which plays a fundamental role in the mapping of connectivity in the brain. With platforms like the Human Connectome Project, where multi-modality imaging data (including diffusion MR data) as well as behavioral and genetic information collected from over a thousand subjects are made available, our ability to detect subtle links between human brain connectivity patterns, genetics and behavioral diversities can be significantly enhanced. In addition to assisting the study of brain circuitry, the reconstruction of EAPs could also open the possibilities of diffusion imaging being used in the investigation of neural developments in numerous disorders and neuroplastic changes following CNS injuries. One such example is the study of spinal cord injury (SCI), which will be further discussed in one of the experiments presented in this paper.

Numerous methods have been proposed to take on the challenge of accurate EAP estimation from dMRI data (Özarslan et al., 2006; Jian et al., 2007; Descoteaux et al., 2011; Merlet et al., 2013; Rathi et al., 2014; Özarslan et al., 2013; Fick et al., 2016). We refer interested readers to recent surveys (Assemblal et al., 2011; Daducci et al., 2014) for further reading. Methods that model the diffusion signal in different ways can also be used to compute the EAP using the above described Fourier transform relation, details of which can be found in a comprehensive survey on compartmental modeling methods (Panagiotaki et al., 2012). Most of these techniques either assume a known model in which case, the basis functions for reconstruction are predefined or in the case of the model free approaches, the positivity constraints on the EAP have to be explicitly enforced, which in some works was not done. In our work here, we take a fresh patch-based dictionary learning approach to this problem. This approach will move away from the requirement of pre-specifying the basis functions and hence is more flexible. Further, the utilization of the square root parameterization of the EAP enables us to incorporate the intrinsic manifold structure of the unit Hilbert sphere in the reconstruction process and produce a non-negative EAP reconstruction without resorting to any explicit constraint enforcement. Last but not least, a patch-based formulation was employed which further enhances the spatial smoothness in the reconstruction.

In the following, we present a brief review of relevant non-linear dictionary learning algorithms and the state-of-the-art in dictionary based EAP reconstruction techniques.

### 1.1. Dictionary learning on Riemannian manifolds: Literature review

Dictionary learning (DL) or sparse coding, which involves representing data as a linear combination of a small number of atoms from the dictionary, has been proven very effective in various image processing tasks (Aharon et al., 2006) as well as dMRI analysis tasks, such as super resolution generation (Yoldemir et al., 2014), image reconstruction from  $\mathbf{k}$ -space data (Song et al., 2014) and EAP reconstruction, which we shall discuss in detail in the following section. In these tasks, learning a dictionary that adapts well to the data is of great importance for a good performance of the sparse representation. Therefore, properly incorporating the geometric structure of the data space is critical to the success of dictionary learning. Several existing dictionary learning algorithms assume that the data points and the atoms are vectors residing in a Euclidean space, and the dictionary is learned based on the vector space structure of the input data (see (Elad, 2010)

and references therein). However, the data used in many medical image analysis tasks often live on Riemannian manifolds such as the space of, symmetric positive definite (SPD) matrices (Moakher, 2005; Wang and Vemuri, 2005; Lenglet et al., 2006; Pennec et al., 2006; Fletcher and Joshi, 2007; Xie et al., 2010) and square root densities (Sun et al., 2013; Ncube and Srivastava, 2011; Çetingül and Vidal, 2011). Therefore, the existing extrinsic approaches that overlook the potentially important intrinsic geometric structure of the data space can exhibit less accuracy in the context of such applications. The issue of accuracy of representation or reconstruction becomes especially evident when the data on the manifold have a large variance. Intuitively, this is obvious and can be easily illustrated in the case of data lying on the upper (lower) hemisphere. Using an extrinsic metric such as the Euclidean metric for computations in this case amounts to ignoring the curvature of the sphere. This is acceptable only when data are tightly clustered around the point of linearization of the manifold and not acceptable when the data have a large variance.

Recently, a provably convergent algorithm was presented in Sun et al. (2015) for the recovery of a complete dictionary from vector-valued data. This was formulated as an optimization problem with a spherical constraint and solved using a Riemannian trust region algorithm over the sphere. Another category of methods seek to solve the dictionary learning problem specifically for data residing on a manifold and are more relevant to the problem addressed in this paper. Yet the majority of these methods are designed for specific manifolds such as the manifold of SPD matrices (Cherian and Sra, 2014; Wu et al., 2015; Sivalingam et al., 2015) and the Grassman manifold. Naturally, these manifold-specific methods, while effective in their respective contexts, are typically difficult to generalize to other Riemannian manifolds. More recently, in Harandi and Salzmann (2015), the authors introduced a Riemannian coding framework that makes use of kernels. However, the successful application of this approach requires one to define/construct positive definite kernels on the Riemannian manifold of interest, which may not be easy in general (Feragen et al., 2015). In contrast, our dictionary learning formulation is applicable to any Riemannian manifold with known or easy to compute the Riemannian exponential (exp) and logarithmic (log) maps (Lee, 1997).

In general, dictionary learning in the Euclidean setting can be formulated as  $\min_{c_1, \dots, c_n, D} \sum_{i=1}^n \|s_i - Dc_i\|^2 + \mathbf{Sp}(c_i)$ , where  $s_1, \dots, s_n$  denotes the given collection of data points,  $D$  is the matrix with columns consisting of the atoms  $a_i$ ,  $c_i$  the sparse coding coefficients and  $\mathbf{Sp}(c_i)$  the sparsity promoting term. One of the key difficulties in generalizing dictionary learning to Riemannian manifolds is to make sure that the collection of atoms as well as the approximation of the data points generated using the atoms still lie on the manifold. The reason is that, in Euclidean space, it is the global linear structure that guarantees the data approximated by a linear combination of the atoms resides in the same space, whereas on Riemannian manifolds, the Riemannian geometry provides only local linear structures through the Riemannian exp and log maps. However, by taking advantage of this diversity of linear structures, it is possible to formulate the dictionary learning problem on Riemannian manifolds in a data specific way. The formulation will be discussed in detail in subsequent sections. It suffices to say that we employ the Riemannian exp and log maps – which are well defined within a neighborhood defined by the injectivity radius of the manifold (Afsari, 2011) – along with an affine constraint to achieve this goal.

### 1.2. Dictionary based EAP reconstruction: Literature review

Dictionaries have long been incorporated in EAP reconstruction techniques in the dMRI community. Existing dictionary based

approaches either involves the design/learning of a dictionary to sparsely represent the diffusion signal or one that is intended for the representation of the EAP.

### • Dictionaries for signal representation.

#### 1. Pre-defined dictionaries.

One sub-category of these signal-oriented dictionary based methods assume a fixed known model for the diffusion signal, in which case the dictionary consists of a set of pre-defined basis. In existing literature, basis that have been utilized in such settings include diffusion basis function (DBF) (Özarslan et al., 2006; Ye et al., 2016), Spherical Ridgelets (SR) (Michailovich and Rathi, 2010), Spherical Harmonics (SH) (Descoteaux et al., 2009), SHORE basis (Özarslan et al., 2008; 2013; Fick et al., 2016), Spherical Polar Fourier (SPF) basis and SPF-dual (Assemblal et al., 2009; Cheng et al., 2010; Merlet and Deriche, 2013). In these methods, following the fitting and reconstruction of the signal, the EAP/ ODF (orientation distribution function, which is a radial projection of the EAP) is calculated (numerically or analytically) from the coefficients of the fitted model. On a less relevant note, one recent development in the compressed sensing (CS) of the  $(\mathbf{k}, \mathbf{q})$ -space of dMRI (Schwab et al., 2016) loosely falls in this category. In an effort to achieve higher acceleration in CS, the authors proposed a joint spatial-angular domain basis using spherical ridgelet/wavelet basis pair for the sparse representation of a field of diffusion signals.

Strictly speaking, these methods do not learn the dictionary atoms (basis) from the data. Hence the performance is heavily dependent on the choice of the basis family and thus compromising the flexibility of the model.

Several approaches in this category stood out owing to their ability to produce non-negative EAP/ ODF reconstruction. For instance, in Schwab et al. (2012) the authors modeled the ODF with Spherical Harmonic (SH) basis and enforced non-negativity on the continuous domain by imposing a positive semi-definiteness constraint on the Toeplitz-like matrices constructed from the SH representation. Cheng et al. (2012) proposed to reconstruct the ODF/ EAP by first estimating the so-called wave function, i.e. the square root of the ODF/ EAP, directly from the diffusion signals, ensuring non-negativity. However, like the rest of the methods based on fixed basis, these two methods lack full data-adaptivity.

#### 2. Semi-adaptive dictionaries.

To circumvent the limitations of fixed dictionary atoms, several approaches were proposed that utilize semi-adaptive dictionaries. In Ye et al. (2012b), an over-complete dictionary based approach was presented to reconstruct EAPs from single shell dMR acquisition. In this approach, adaptive spline kernels were used for the modeling of the dMR signal and the EAPs were estimated post signal reconstruction. In Merlet et al. (2013), proposed a Spherical Harmonic basis function based parametric dictionary learning framework that leads to an analytical reconstruction of the EAPs and ODFs from the dMRI data. DL-SPFI was proposed in Cheng et al. (2013) to learn a dictionary consisting of SPF basis with the scale value adaptively set based on the mean diffusivity of the diffusion signals. More recently, the same group proposed a generalization of DL-SPFI named DL-TSPFI (Cheng et al., 2015), by considering general adaptive tensor setting instead of the scalar case. Another recent development in the same vein was reported in Aranda et al. (2015). The authors designed an adaptive diffusion dictionary method based on the DBF model for the reconstruction of the MR signal, where the dictionary

atoms are iteratively re-estimated independently at each voxel. Even though EAP reconstruction was not the focus of this particular work, one can easily estimate the EAPs analytically from the reconstructed signal represented in DBFs. Despite their efforts to adapt the atoms to the particular data of interest, the majority of these techniques were still built upon a particular model for the diffusion signal and only certain parameters of the model are fully flexible and learned in the parametric framework. Further, the post signal reconstruction EAP/ ODF estimation provides no guarantees for the non-negativity of the probability functions.

#### • Dictionaries for EAP/ ODF representation.

The second category of dictionary based techniques aim to utilize a dictionary specifically designed for the EAPs to achieve direct EAP reconstruction without resorting to first fitting a model to the diffusion MR signal.

Bilgic et al. (2013), proposed to learn a discrete dictionary via the K-SVD algorithm on a training set of EAPs, and showed that this dictionary can be used in a CS framework to accelerate the DSI technique for efficient direct reconstruction of the EAPs. However, neglecting the geometric structure of the space in which the EAPs live, this method cannot ensure the non-negativity of the reconstructed EAPs, which is an intrinsic and basic property of the EAPs. Accordingly, it is prone to higher numerical errors. Recently, in a conference version of the current manuscript, we reported some preliminary results of applying a non-linear DL approach for the EAP reconstructions from multi-shell dMRI in Sun et al. (2013), wherein the dictionary atoms are fully adaptive and the non-negativity of the reconstructed EAPs is guaranteed. Yet, the dictionary, though learned over the entire field, was designed for the sparse representation of individual (at each voxel) EAPs. However, there is no guarantee of a spatially smooth reconstruction without the incorporation of an explicit spatial regularization term.

Distinct from the conference version (Sun et al., 2013) of this manuscript, in this paper, we move away from voxel-wise reconstruction which was widely used in existing methods and consider the reconstruction of the EAP field in a patch-based manner. Patch-based dictionary learning is well studied in the context of image denoising, inpainting, super-resolution etc. Our patch-based algorithm is inspired by the success achieved in the task of image reconstruction in compressed sensed MRI via patch-based linear dictionaries reported in Ravishankar and Yoram (2011). We propose to apply a general non-linear dictionary learning method on the product manifold of Hilbert spheres where the patches of square root of EAPs reside. As a result, in addition to ensuring the non-negativity of the reconstructed EAPs, our approach also achieves a spatially regularized reconstruction, which can be extremely valuable in practice especially when the data are noisy. We first demonstrate this point on noise contaminated synthetic data through quantitative and qualitative evaluations. Further, we showcase the potential of our method in assisting the studies of white matter micro-structures in the CNS through experiments on HCP human brain data and rat spinal cord data.

To demonstrate the significance of respecting the intrinsic geometric structure of the manifold the square root of EAPs reside on, we compare our method to linear dictionary learning based EAP reconstruction techniques (Aharon et al., 2006; Ye et al., 2012b). Note that the linear dictionary learning method in Aharon et al. (2006) is a patch-based method and uses the KSVD algorithm. Hence, our method can be seen as a generalization of this patch-based linear DL method. We also include comparisons with the state-of-the-art EAP/ ODF reconstruction approach MAPL (Fick et al., 2016) (non-dictionary based) to showcase the superior performance of our method in the context of the angular recovery

accuracy. Further, we compute an imaging biomarker based on an entropic anisotropy measure which is a function of the well known Rényi entropy. Using a statistical two-sample  $t$ -test, we demonstrate its efficacy in discriminating and identifying the regions of significance between control and injured cords at sites distant from the injury.

The rest of the paper is organized as follows. Section 2 contains mathematical preliminaries of Riemannian manifolds, the dictionary learning formulation and relevant basics on the two Riemannian manifolds of interest for our application. In Section 3, we present a detailed description of the synthetic, phantom and real data sets used in testing the proposed patch-based dictionary learning and reconstruction algorithm. We present several experimental results on synthetic and real data sets in Section 4 and draw conclusions in Section 6.

## 2. Theory

### 2.1. Mathematical preliminaries of Riemannian manifolds

In this section, we review some basic concepts on Riemannian manifolds and refer the interested readers to Spivak (1979); Lee (1997) for more details. A topological space that is locally homeomorphic to open subsets of the Euclidean space  $\mathbb{R}^d$  at each point is called a manifold  $\mathcal{M}$  of dimension  $d$ . Manifold  $\mathcal{M}$  becomes a differentiable manifold when it has a differential structure globally defined on it. The global differential structure makes possible the definition of the globally differentiable tangent space.  $T_p\mathcal{M}$ , the tangent space at a point  $p \in \mathcal{M}$ , is a vector space that consists of all the tangent vectors to  $\mathcal{M}$  at  $p$ . A Riemannian manifold is defined as a differentiable manifold on which each tangent space  $T_p\mathcal{M}$  is equipped with a differentiable varying inner product  $\langle \cdot, \cdot \rangle_p$ . The geodesic curve  $\gamma : [0, 1] \rightarrow \mathcal{M}$  is a smooth curve of minimal length connecting any two points on the manifold. We refer the reader to Afsari (2011) for details on the conditions for uniqueness of geodesics. Consider a tangent vector to the manifold at a point  $p$ ,  $v \in T_p\mathcal{M}$ , there exists a unique geodesic  $\gamma_v$  satisfying  $\gamma_v(0) = p$  with initial tangent vector  $v$ . The exponential map  $\exp_p : T_p\mathcal{M} \rightarrow \mathcal{M}$  of  $v$  is defined as  $\exp_p(v) = \gamma_v(1)$ . The logarithmic map, denoted as  $\log_p : \mathcal{M} \rightarrow T_p\mathcal{M}$  is the inverse of the exponential map. Fig. 1 depicts an intuitive illustration of these maps at a point on a manifold.

Let  $p_i$  and  $p_j$  be two points on  $\mathcal{M}$ ,  $\log_{p_i}(p_j)$  maps point  $p_j$  to the unique tangent vector at  $p_i$  that is the initial velocity of the geodesic  $\gamma$  with  $\gamma(0) = p_i$  and  $\gamma(1) = p_j$ . Conditions for existence of these maps are elaborated upon in Pennec et al. (2006). The geodesic distance between  $p_i$  and  $p_j$  is  $\text{dist}(p_i, p_j) = \|\log_{p_i}(p_j)\|_{p_i}$ . Here, the notation  $\|\cdot\|_{p_i}$  indicates the induced norm at the point  $p_i$ .

### 2.2. Dictionary learning on Riemannian manifold

Given a collection of signals  $s_1, \dots, s_n \in \mathbb{R}^d$ , the classical dictionary learning methods in a Euclidean setting (Aharon et al., 2006)

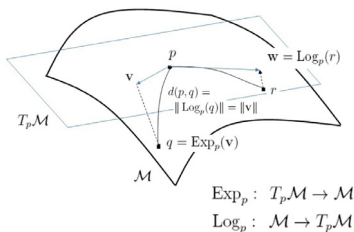


Fig. 1. Illustration of the Riemannian log and exponential maps.

seek to find a dictionary  $D \in \mathbb{R}^{d \times m}$  whose columns are composed of  $m$  atoms that can sparsely approximate each signal  $s_i$  as a linear combination  $s_i \approx Dc_i$ , where  $c_i \in \mathbb{R}^m$  is the coefficient vector. Applying  $l_1$  regularization on  $c_i$ , the dictionary learning problem can be formulated as:

$$\min_{c_i, D} \sum_{i=1}^n (\|s_i - Dc_i\|_2^2 + \lambda \|c_i\|_1) \quad (2)$$

where  $\lambda$  is a regularization parameter.

Let  $s_1, \dots, s_n \in \mathcal{M}$  be a collection of  $n$  data points on manifold  $\mathcal{M}$ , and let  $a_1, \dots, a_m \in \mathcal{M}$  be the atoms of the learned dictionary  $\mathcal{D} = \{a_1, \dots, a_m\}$ . In the Riemannian manifold setting, due to the local linear geometric structure of  $\mathcal{M}$ , it is unsuitable to directly use the linear combination of the atoms  $\hat{s}_i = \sum_{j=1}^m c_{ij}a_j$  to represent the data  $s_i$ , since there is no guarantee that such an  $\hat{s}_i$  still resides on the manifold. Instead, by adopting the geodesic linear interpolation on  $\mathcal{M}$ ,  $s_i$  can be approximated by

$$\hat{s}_i = \exp_{s_i} \left( \sum_{j=1}^m c_{ij} \log_{s_i}(a_j) \right) \quad (3)$$

where,  $\exp_{s_i}$  and  $\log_{s_i}$  are the exponential and logarithmic maps (defined earlier) respectively at  $s_i$ , and  $c_{ij} \in \mathbb{R}$  are the coefficients. Intuitively speaking, we project all the atoms in the dictionary to the tangent space at  $s_i$ , the data point to be approximated, and construct the linear combination  $v_i = \sum_{j=1}^m c_{ij} \log_{s_i}(a_j)$  in the tangent space  $T_{s_i}\mathcal{M}$ , then we obtain the approximation  $\hat{s}_i$  by taking the exponential map of  $v_i$  at  $s_i$ .

Our goal is to construct a dictionary that minimizes the sum of the reconstruction error over all data point which is defined as  $E_{\text{data}} = \sum_{i=1}^n \text{dist}(s_i, \hat{s}_i)^2 = \sum_{i=1}^n \|\log_{s_i}(\hat{s}_i)\|_{s_i}^2 = \sum_{i=1}^n \|\sum_{j=1}^m c_{ij} \log_{s_i}(a_j)\|_{s_i}^2$ . Imposing the  $l_1$  sparsity constraint, we formulate the dictionary learning problem on the manifold  $\mathcal{M}$  as the following optimization problem,

$$\begin{aligned} \min_{C, D} \sum_{i=1}^n \left\| \sum_{j=1}^m c_{ij} \log_{s_i}(a_j) \right\|_{s_i}^2 + \lambda \|\text{vec}(\mathbf{C})\|_1 \\ \text{s.t. } \sum_{j=1}^m c_{ij} = 1, i = 1, \dots, n. \end{aligned} \quad (4)$$

Where,  $\mathbf{C} \in \mathbb{R}^{n \times m}$  and the  $(i, j)^{\text{th}}$  entry of  $\mathbf{C}$  is denoted as  $c_{ij}$ .  $\text{vec}(\mathbf{C})$  here corresponds to the vectorized form of the matrix  $\mathbf{C}$ . Note that a similar data term was used in Çetingül and Vidal (2011) but the atoms were assumed fixed. The affine constraint in our formulation implies that affine subspaces are used to approximate the data instead of the usual subspaces, which are simply affine subspaces based at the origin. Generalizing from Euclidean spaces to Riemannian manifolds, there exists no corresponding notion of the origin to define the usual subspaces, and this geometric fact requires one to discard the usual subspaces in favor of general affine subspaces. It is worth noting that explicit normalization on the atoms is not needed in this formulation. Due to the incorporation of the manifold structure of the square root densities, the atoms learned in our approach are always on the hypersphere, while in the traditional dictionary learning (Eq. (2)) a normalization is required to guarantee the unique solution. Similar to the traditional dictionary learning methods, we use an iterative (alternating) method to solve this optimization problem where each iteration consists of two steps: (1) sparse coding step (for a fixed dictionary  $\mathcal{D}$ , optimize with respect to the coefficients  $\mathbf{C}$ ), (2) codebook optimization step (for fixed  $\mathbf{C}$  optimize with respect to  $\mathcal{D}$ ). It should be noted that this alternating (two stage) method of solving the problem in the traditional vector-space setting (Eq. (2)) does not provide convergence guarantees to the global optimum (Aharon et al., 2006).

However, this approach has had significant success in many practical applications such as, denoising, in painting and classification (Aharon et al., 2006; Elad, 2010).

The first step is a regular sparse coding (convex) problem that can be easily solved using many existing fast algorithms. We use the CVX solver for this step in this work. However, the second subproblem of updating the dictionary is much more challenging, since the optimization techniques designed in Euclidean space are not appropriate for the optimization problem on manifolds. We propose to adopt the line search algorithm on Riemannian manifold introduced in Absil et al. (2008) to update the dictionary  $\mathcal{D}$ . We first initialize the atoms in the dictionary with the  $m$  clusters of the data  $s_1, \dots, s_n$  generated by a K-means algorithm applied to all the data. Then, we apply the aforementioned line search algorithm to optimize the cost function. Intuitively, the idea is to find a descent direction  $\mathbf{v}$  on the tangent space anchored at each atom, and take a step along the geodesic  $\gamma$  whose initial velocity is  $\mathbf{v}$ . The algorithmic details and the convergence analysis of the line search method on manifolds are discussed in Absil et al. (2008).

### 2.3. Manifold of square root density functions

In this section, we present some relevant concepts pertaining to the manifold of square root density functions (i.e. unit Hilbert sphere), which is essential to understanding the structure of the product manifold. Without loss of generality, we restrict the analysis to probability density functions (PDFs) defined on the interval  $[0, T]$  for the purpose of simplicity.

The manifold of square root density functions is defined as  $\Psi = \{\psi : [0, T] \rightarrow \mathbb{R} \mid \forall s, \psi(s) \geq 0, \int_0^T \psi^2(s) ds = 1\}$ . As we can see,  $\Psi$  forms a convex subset of the unit sphere in a Hilbert space. The Fisher-Rao metric can be obtained as  $\langle v, w \rangle_x = \int_0^T v(s)w(s)ds$ , where  $v, w \in T_x\Psi$  are tangent vectors at  $x$ . Let  $x, y \in \Psi$  be two arbitrary square root density functions, the geodesic distance between them is given in closed form by  $\text{dist}(x, y) = \cos^{-1}(\langle x, y \rangle)$ , which is simply the angle between  $x$  and  $y$  on the unit hypersphere. The geodesic at  $x$  in direction  $v \in T_x\Psi$  is defined as  $\gamma(t) = \cos(t)x + \sin(t)\frac{v}{|v|}$ . The exponential map can be computed as  $\text{exp}_x(v) = \cos(|v|x) + \sin(|v|)\frac{v}{|v|}$ . Here, we restrict  $|v| \in [0, \pi)$  to ensure that the exponential map is a bijection. The logarithmic map is then given by  $\text{log}_x(y) = u \cos^{-1}(\langle x, y \rangle) / \sqrt{\langle u, u \rangle}$ , where  $u = y - \langle x, y \rangle x$ . Note that the Riemannian log and exp maps and the geodesics are uniquely defined on the sphere within the injectivity radius  $\pi/2$ . Further, the data are assumed to lie within the ball of this radius as is usually the case in practice.

### 2.4. Product manifold of square root density functions

Owing to the generality of the proposed dictionary learning formulation on various types of Riemannian manifolds, we can apply it to patches of EAPs where each EAP is represented by a square root density function. These patches can be treated as points on the product manifold of square root density functions. We now present the geometry of this manifold. Following the notation from last section, a square root density field defined on a domain  $\Omega$  in  $\mathbb{R}^K$  can be represented as a function  $f: \Omega \rightarrow \Psi$ . In most medical image analysis applications, the square root density fields are defined over a grid (pixels or voxels), thus  $\Omega$  will be a collection of  $m$  points in  $\mathbb{R}^K$ . We identify the space of square root density fields on  $\Omega$  with the  $m$ -fold Cartesian product  $\Psi^m = \Psi \times \Psi \times \dots \times \Psi$ . Hence a square root density field  $\mathbf{X}$  in  $\Psi^m$  can be represented as an  $m$ -tuple  $(x_1, x_2, \dots, x_m)$ , where each  $x_i$  is a square root density function, the value of  $\mathbf{X}$  at the  $i$ th voxel in  $\Omega$ .

Given  $(\mathcal{M}_1, g_1)$  and  $(\mathcal{M}_2, g_2)$  as Riemannian manifolds with corresponding metrics, the product space  $\mathcal{M}_1 \times \mathcal{M}_2$  has a natural Riemannian metric  $g = g_1 \oplus g_2$ , called the product metric,

defined by  $g(v_1 + v_2, w_1 + w_2) = g_1(v_1, w_1) + g_2(v_2, w_2)$ , where  $v_i, w_i \in T_{p_i}\mathcal{M}_i$  under the natural identification  $T_{(p_1, p_2)}\mathcal{M}_1 \times \mathcal{M}_2 = T_{p_1}\mathcal{M}_1 \oplus T_{p_2}\mathcal{M}_2$  (Lee, 1997). This can be generalized to our  $m$ -fold product space  $\Psi^m$ . Let  $\mathbf{V}, \mathbf{W} \in T_{\mathbf{X}}\Psi^m$  be two tangent vectors at  $\mathbf{X} \in \Psi^m$ , the product Riemannian metric gives the inner product between the two vectors as  $\langle \mathbf{V}, \mathbf{W} \rangle_{\mathbf{X}} = \sum_{i=1}^m \langle v_i, w_i \rangle_{x_i} = \sum_{i=1}^m \int_0^T v_i(s)w_i(s)ds$ , where  $v_i, w_i \in T_{x_i}\Psi$ . Using this metric, the exponential map at  $\mathbf{X}$  maps the tangent vector  $\mathbf{V}$  to a point in  $\Psi^m$

$$\text{Exp}_{\mathbf{X}}(\mathbf{V}) = \left( \cos(|v_1|x_1) + \sin(|v_1|)\frac{v_1}{|v_1|}, \dots, \cos(|v_m|x_m) + \sin(|v_m|)\frac{v_m}{|v_m|} \right)$$

Given  $\mathbf{X} \in \Psi^m$ , the Riemannian log map anchored at  $\mathbf{X}$  is,

$$\text{Log}_{\mathbf{X}}(\mathbf{Y}) = \left( u_1 \cos^{-1}(\langle x_1, y_1 \rangle) / \sqrt{\langle u_1, u_1 \rangle}, \dots, u_m \cos^{-1}(\langle x_m, y_m \rangle) / \sqrt{\langle u_m, u_m \rangle} \right).$$

Where,  $u_i = y_i - \langle x_i, y_i \rangle x_i$  for  $i = 1, \dots, m$ . Using this definition of Riemannian log map, the geodesic distance between two square root density fields  $\mathbf{X}$  and  $\mathbf{Y}$  is computed by,  $\text{dist}(\mathbf{X}, \mathbf{Y}) = \|\text{Log}_{\mathbf{X}}(\mathbf{Y})\| = \sqrt{\sum_{i=1}^m (\cos^{-1}(\langle x_i, y_i \rangle))^2}$ .

### 2.5. Reconstruction of EAP fields

In this section, we describe the pipeline of our EAP field reconstruction framework based on the dictionary learning algorithm presented herein.

Given a set of dMR signals (within a 2-D slice or 3-D volume), we first compute an initial estimate of the EAPs in a voxel-wise manner, for which any approach of choice can be used. In this work, we use different initializations namely, methods proposed in Jian et al. (2007); Ye et al. (2012a); Fick et al. (2016); Wedeen et al. (2005). The method in Jian et al. (2007) was used for single shell data since the implementation is only available for single shell data sets. The MAPL method in Fick et al. (2016) was used both for single and multi-shell data sets and the method from Ye et al. (2012a) was used for multi-shell data. The method from Wedeen et al. (2005) was used with DSI data. Following the initial estimation, the square root parameterization is taken for each EAP vector at individual voxels. Then we extract overlapping patches of the square root density representation of the EAPs and learn a dictionary (that consists of atoms living on the product manifold of unit Hilbert spheres) from these patches. Subsequently, the square root of each EAP patch can be represented by a non-linear combination (Eq. (3)) of the learned atoms, and the corresponding EAPs are obtained by squaring the reconstructed roots. For a voxel that belongs to  $k$  different patches, there exists a set of  $k$  estimates of the EAP. Finally, we reconstruct the EAP at every voxel by aggregating these set of estimates. The aggregation involves averaging the EAP estimates at the overlapping voxel locations. This can be achieved using the Fréchet mean of the EAP estimates or if the estimates are very close in geodesic distance, an arithmetic mean followed by a projection to the manifold of densities will prove to be sufficiently accurate and very efficient. In this work, we used the latter approach. A flow chart illustrating the pipeline of our EAP reconstruction framework is presented in Fig. 2.

### 2.6. Renyi entropy: An imaging 'Stain'

Fig. 2 depicts the end-to-end pipeline for computing the proposed imaging biomarker/ 'stain' from an input diffusion MR image. We now describe the last stage of the pipeline namely, the computation of the scalar anisotropic index (HA) from the reconstructed EAPs. HA is related to the well known Rényi entropy from

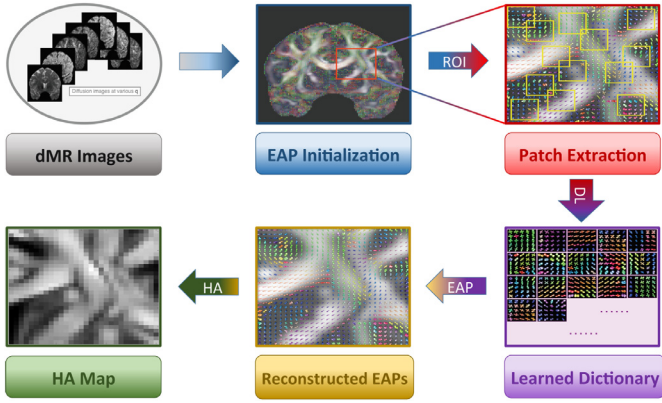


Fig. 2. Pipeline of the proposed EAP reconstruction framework.

information theory (Rényi, 1961). Rényi entropy defines a family of entropies and was proposed by Rényi (1961). Rényi entropy is analogous in some sense to  $L_p$  norms and can be interpreted geometrically using the language of these well studied norms. The reason one considers  $L_p$  norms is that they give us a continuous trade-off between the extremes  $L_0$  and  $L_\infty$ . Shannon entropy is analogous to the  $L_1$  norm, it tells us the average information but nothing about the variances or the extremes. The min-entropy (also called Chebyshev entropy), analogous to the  $L_\infty$  norm, gives us the information on the element with the largest probability and nothing about the rest. The other extreme, analogous to the  $L_0$  norm, being simply the logarithm of the number of nonzero components of the distribution i.e., the support of the distribution (also called Hartely's entropy). Rényi entropy provides a continuous one parameter family of entropies between the two extremes. Since its inception, it has found numerous applications in variety of fields including but not limited to cryptography, fractal geometry and ecology.

The Rényi entropy of order  $\alpha$  is defined as,

$$H_\alpha(X) = \frac{1}{1-\alpha} \log \left( \sum_{i=1}^n p_i^\alpha \right), \quad (5)$$

where,  $\alpha \geq 0$  and  $\alpha \neq 1$ ,  $X$  is a discrete random variable, obtained from the reconstructed EAP in this paper, with probabilities  $\{p_i\}_{i=1}^n$ , and the logarithm is to base 2. Rényi entropy generalizes the Hartley or max entropy  $H_0(X)$ , the Shannon entropy  $H_1(X)$  (in the limit  $\alpha \rightarrow 1$ ), the collision entropy  $H_2(X)$  and the min entropy  $H_\infty(X)$ . It is evident from the definition that, whereas  $H_0(X)$  weighs all possible events equally and depends only on the size of the support of  $X$  ( $n$ ),  $\alpha \rightarrow \infty$  only depends on the events of highest probability. For the spinal cord data, since we have two classes, control and moderate injury, in each voxel, we estimate the optimal  $\alpha \geq 0$  to provide the best possible discrimination between the two injury groups. Here discrimination is achieved using the standard two sample t-test.

In this paper, the Rényi entropy computed from the EAPs measures the uncertainty of the water diffusion process, which in turns can be used to quantify anisotropy at each voxel. Low entropy signifies anisotropic diffusion, whereas high entropy shows isotropic diffusion. We computed an anisotropic measure (HA) from the Rényi entropy as defined in McGraw and Vemuri (2005), which will serve as an imaging stain. This measure is defined as,

$$HA = \left( 1 - \frac{H_\alpha(X)}{\log n} \right)^\beta, \quad (6)$$

where, the parameter  $\beta$  controls the contrast between white and grey matter. In diffusion MR images, isotropic diffusion results in high entropy and hence low HA value (mapped to low gray values)

while anisotropic diffusion leads to low entropy and hence high HA value (mapped to high gray values). HA can thus serve as a useful quantitative measure i.e., an imaging stain/ biomarker, that can be used to capture anisotropic changes possibly caused by pathology. Note that unlike fractional anisotropy (FA) which can only be computed for the diffusion tensor models, HA is not restricted to the type of model used to represent the diffusivity function, since it is computed from the EAP which is the Fourier transform of the diffusion sensitized MR signal. Accuracy of HA computation is directly dependent on the accuracy of EAP estimation. Further, HA is easy to compute and does not require the EAPs to be parametrically represented in a basis. Note that HA does not have a pre-disposition toward any particular EAP estimation method. This is because, HA is based on Rényi entropy which is not biased toward the shape of any probability density function. Further, unlike existing scalar measures of anisotropy such as RTAP (return to axis probability) and RTPP (return to plane probability) (Özarslan et al., 2013), which require estimating the direction of the assumed cylindrical fiber model using a diffusion tensor fitting technique that could yield erroneous prediction in the presence of crossing fiber bundles, HA does not require any such estimates. This justifies HA as an unbiased measure of entropy-based anisotropy index and its use as a possible biomarker in our experiments.

Based on this biomarker, we performed a statistical test to compare the ability of the reconstructed EAPs from various methods to differentiate the injured from control rat spinal cords. With the computed entropy fields, we carried out a two-sample  $t$ -test with significance level 0.10. The resulting significant regions indicated by voxels with p-values less than (0.10) are useful in visualizing the extent of the effect of the injury to various regions of the spinal cord.

### 3. Materials and methods

#### 3.1. Implementation

Our patch-based DL algorithm is implemented using a combination of the CVX package for convex optimization and a line search technique on Riemannian manifolds. The former is used to solve the convex optimization problem to find the weights for fixed dictionary atoms and the latter is used for optimizing on the dictionary atoms for fixed weights. With regards to our patch-based DL algorithm, size of patches in our experiments ranged over (3,3,3), (5,5,5) and (7,7,7), respectively and the overlap between patches (i.e., stride) is set to 2 in all our experiments in the paper. Number of patches is a function of the size of the image, size of patches and amount of overlap. The number of dictionary elements/atoms in our experiments ranged over 50 to 200 in increments of 50. All the parameter values were chosen based a grid search technique to yield the best performance for the data at hand.

The proposed approach and competing methods (except for MAPL, written in Python) were implemented in Matlab and all computations were performed on a workstation with a Intel Core(TM) i7 CPU930 2.80 GHz  $\times$  8 processor and a 24 GB RAM. The CPU time taken for all our experiments vary over the range of half hour to three and half hours. Our code however is developed in MATLAB and is not optimized in any way. Finally, we would like to mention that all the figures in color are accessible to the readers in the online version of the paper.

#### 3.2. Description of data sets

We perform comprehensive evaluation of our method on various types of diffusion data, including single-shell HARDI, multi-shell HARDI as well as DSI. The data pool consists of a synthetic dataset with complex fiber configurations, a realistic chal-



**Fig. 3.** Illustration of fiber structures in the phantom (figure from Daducci et al. (2013)).

lence phantom dataset that has been previously validated by various methods and two real diffusion datasets acquired from human brain and rodent spinal cords respectively.

### 3.2.1. Synthetic data

We synthesized diffusion signals in a slice of size  $24 \times 24$  simulating two straight fiber bundles crossing each other in the center with a circular fiber bundle passing through at the corners. The ground-truth EAP profiles are presented in Fig. 5 (top row). The signals were generated using the ball and stick model in the Camino diffusion MRI toolkit (Cook et al., 2006). The diffusion parameters used in a typical HCP dataset (latest release) were used for the data simulation, where the diffusion weighting consisted of 3 shells of b-values  $\{1000, 2000, 3000 \text{ s/mm}^2\}$ , with 90 diffusion weighting directions on each shell. In addition to noise-free simulation, we generated Rician noise contaminated version of this dataset with signal-to-noise ratio (SNR) varying from 10 to 30 to evaluate our method's robustness to noise.

### 3.2.2. ISBI HARDI challenge 2013 phantom data

We also perform evaluation of our method on the phantom data provided at the ISBI (IEEE International Symposium on Biomedical Imaging) HARDI challenge 2013. The advantage of employing this data lies in the fact that the phantom is created in a more realistic setting and the ground-truth is available which makes the quantitative assessments of the results possible. The phantom consists of a set of fiber bundles with a wide range of configurations (branching, crossing, kissing), fiber bundles radii, and fiber geometry. The structure of the fibers are shown in Fig. 3 (Daducci et al., 2013).

The diffusion MR signal is simulated in each voxel considering hindered and restricted diffusion, to account for extra-axonal and intra-axonal diffusion. Depending on the position in space, there is also an isotropic compartment, to account for the CSF contamination close to the ventricles in brain imaging. Finally, the magnitude MR signal is corrupted by Rician noise resulting in SNR of 10, 20 and 30 respectively. Three different sampling classes were used for the simulation, namely DTI-like, HARDI-like and DSI. In this experiment, we intend to test the proposed algorithm on data that is acquired with a different sampling scheme than that in the previous dataset, and to further assess its performance on data severely corrupted by noise. Hence, we chose the DSI simulation with an SNR of 10.

### 3.2.3. Wu-Minn HCP human brain data

The HCP HARDI data used in our experiments was collected on a Siemens 3T "Connectome Skyra" scanner. The diffusion weighting consisted of 3 shells of b-values  $\{1000, 2000, 3000 \text{ s/mm}^2\}$ , with

90 diffusion weighting directions on each shell. The images were acquired with 1.25 mm isotropic resolution,  $210 \times 180 \text{ s/mm}^2$  FOV and  $TE/TR = 89.5/5520 \text{ ms}$ .

### 3.2.4. Rat spinal cord data

In the final experiment, we validated our method on diffusion data collected from rat spinal cords to demonstrate the potential of our EAP reconstruction technique in dMRI-based studies of the central nervous system (CNS). In this dataset we have 8 controls and 12 moderately injured rat spinal cords. The rats in the moderately injured group received a contusion with 200 kdyn force applied to the T10 vertebral level of the spinal cord, while the controls have their spinal cords intact (All procedures were approved by the University of Florida Institutional Animal Care and Use Committee, and the methods of anesthesia and spinal cord injury have been described previously (Lane et al., 2012)). The dMR images consist of slices from the cervical (C4) section, which is distant to the injury site. The dMR images were acquired on a Bruker MR scanner at 750MHz (17.6T) with 21 gradient directions at b-value  $1000 \text{ s/mm}^2$ , the voxel size was  $60 \mu\text{m}$  isotropic,  $TE/TR = 20.64/700 \text{ ms}$ .

## 4. Results

### 4.1. Comparisons with the state-of-the-art

To demonstrate the properties of our non-linear DL based EAP field reconstruction approach, we compare it with various EAP reconstruction techniques detailed below.

We compare our approach with (positivity constrained) MAPL (Fick et al., 2016), which is the state-of-the-art technique for EAP/ODF reconstruction from dMRI. MAPL falls in the category of methods that use fixed basis for signal modeling. It achieves signal reconstruction through regularizing the coefficient estimation of the Mean Apparent Propagator (MAP)-MRI model using the norm of the Laplacian of the reconstructed signal, after which the EAP/ODF is analytically computed using the coefficients. Note that authors of Fick et al. (2016); Özarslan et al. (2013) use the term MAP for what we and others in literature call EAPs. The non-negativity of the reconstructed EAP can also be enforced on the MAPL framework in the same manner as proposed in the positivity constrained MAP-MRI approach (Özarslan et al., 2013). In this paper, we compare our proposed method with this constrained version of MAPL to showcase the superior angular discrimination achieved by our method while maintaining the non-negativity of the EAP reconstruction. The implementation of MAPL with isotropic scaling factors was chosen for our experiments, as the reconstruction of the EAPs is the primary focus of this work and for this particular task, the isotropic version was recommended by the first author of Fick et al. (2016) over the anisotropic setting. However, for the sake of completeness, we also included results obtained with the anisotropic setting as well.

In order to establish the advantage of incorporating the intrinsic geometric structure of the manifolds, we compare our non-linear DL based approach with several linear DL based approaches. (1) As a representative of semi-adaptive dictionary based EAP reconstruction methods, the technique proposed in Ye et al. (2012b) was picked as one of the competing methods. It was briefly discussed in Section 1.2 that this method was implemented for single-shell dMRI data, hence for some of the data examples in the following experiments we had to generalize the implementation to tackle multi-shell acquisitions. In the rest of this paper, we denote this linear DL based EAP reconstruction approach as "YEV" for brevity. (2) We replace the proposed manifold-based DL algorithm with the widely used linear DL algorithm K-SVD (Aharon et al., 2006) in our EAP reconstruction framework described in Section 2.5 (denoted as

K-SVD for short) and compare it with our proposed approach. Note that the K-SVD approach is a patch-based linear DL technique. The purpose of such experiment is to reduce the effect of other confounding variables in the comparison and to ensure that the incorporation of the manifold structure is the only factor contributing to any difference in the performance of the two methods. As a result, this comparison has the potential to reveal more insight into the benefit provided by respecting and incorporating the geometric structure of the data space in the dictionary learning.

In the following, we present and discuss the experimental results on the datasets described previously.

#### 4.2. Synthetic data

We report our findings on the synthetic data in two ways, through visual inspection and quantitative assessment respectively. In the quantitative assessment, we are particularly interested in the comparison of the angular discriminative power of each method. Therefore we investigate the number of peaks detected from the reconstructed EAPs and the estimated crossing angles in the fiber crossing regions. For peak detection, we use the non-linear peak detection module in the open source library Dipy (Garyfallidis et al., 2014), and the crossing angles are estimated as the angle between the largest two peaks detected from the EAP profiles in the crossing area. We would like to point out that in the preliminary results reported in Sun et al. (2013), a different peak detection scheme was used, wherein peaks were obtained by finding the local maximum in a neighborhood of the known ground-truth peaks. This scheme, however, requires knowledge of the ground-truth fiber orientations and tends to lead to underestimation of angular errors.

The proposed approach and all 3 competing methods were applied on the noise-free data and noisy data with various SNRs to reconstruct the EAPs. We estimate the fiber crossing angle at each voxel in the crossing regions from the reconstructed EAP fields and report the average angular error in contrast to the ground-truth crossing angles in Fig. 4. The numerical results show that our proposed method yielded the lowest angular error compared to

the state-of-the-art EAP/ODF reconstruction approach MAPL (with isotropic and anisotropic settings) as well as linear DL based methods at all noise levels (including noise-free). It achieved high accuracy reconstructions on the noise-free data with an average angular error as low as 2 degrees, and maintained considerably high accuracy as the noise level increases. Even for data with high noise contamination (SNR of 10), the angles estimated using our method are still within the range of 9 degrees from the ground-truth on average. It can also be seen that with our approach, the standard deviation of the angular errors in the crossing regions (shown as error bars in the figure) stays relatively low in the presence of noise. On the other hand, MAPL (isotropic setting) performed considerably well on data with low noise, but showed fluctuating behavior in angular accuracy with decreasing SNR. This fluctuation in angular error could be due to the introduction of false peaks detected from the EAP reconstructions using MAPL at high noise level, one example is shown in Fig. 6 for the data with SNR of 15 (the sub-figure on the far right in the third row). Conventional DL based approaches, YEV and K-SVD, overall showed suboptimal performance compared to the proposed method, yet demonstrated better robustness to noise in contrast to non-DL based MAPL.

To better evaluate the quality of the reconstructions, in Fig. 5 we showcase the ground-truth EAP profiles and the reconstructed EAP fields using all 4 techniques for the noise-free data as well as data contaminated with 2 different levels of noise, resulting in an SNR of 15 and 25, respectively. In addition, the number of peaks detected in each reconstructed EAP field are presented in Fig. 6, along with the ground-truth number of peaks. These results verify the observations we made previously, from a visual perspective. As is shown in both figures, reconstructions using the proposed method are of high quality for data with zero to mild level of noise, with respect to the recovery of both EAP profiles and peaks. At a lower SNR, the EAP profiles get smudged and as a result false peaks are detected from the EAP estimates, which is to be expected. Yet, the underlying structure of the fibers in the data can still be observed in the reconstructed EAP field (see the top right sub-figure in Fig. 5). Visually, the overall performance of K-SVD shows a similar pattern as the proposed approach regarding

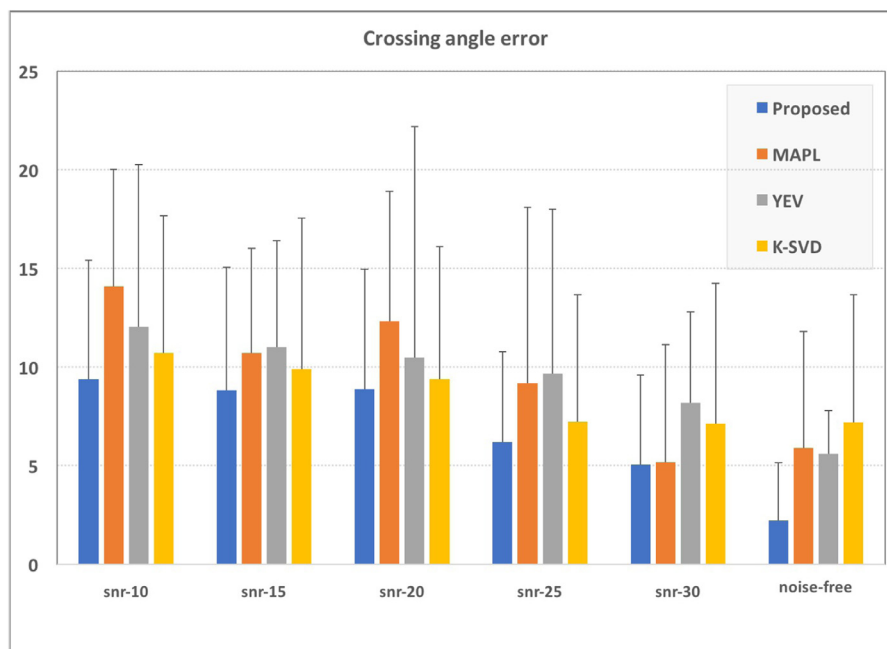
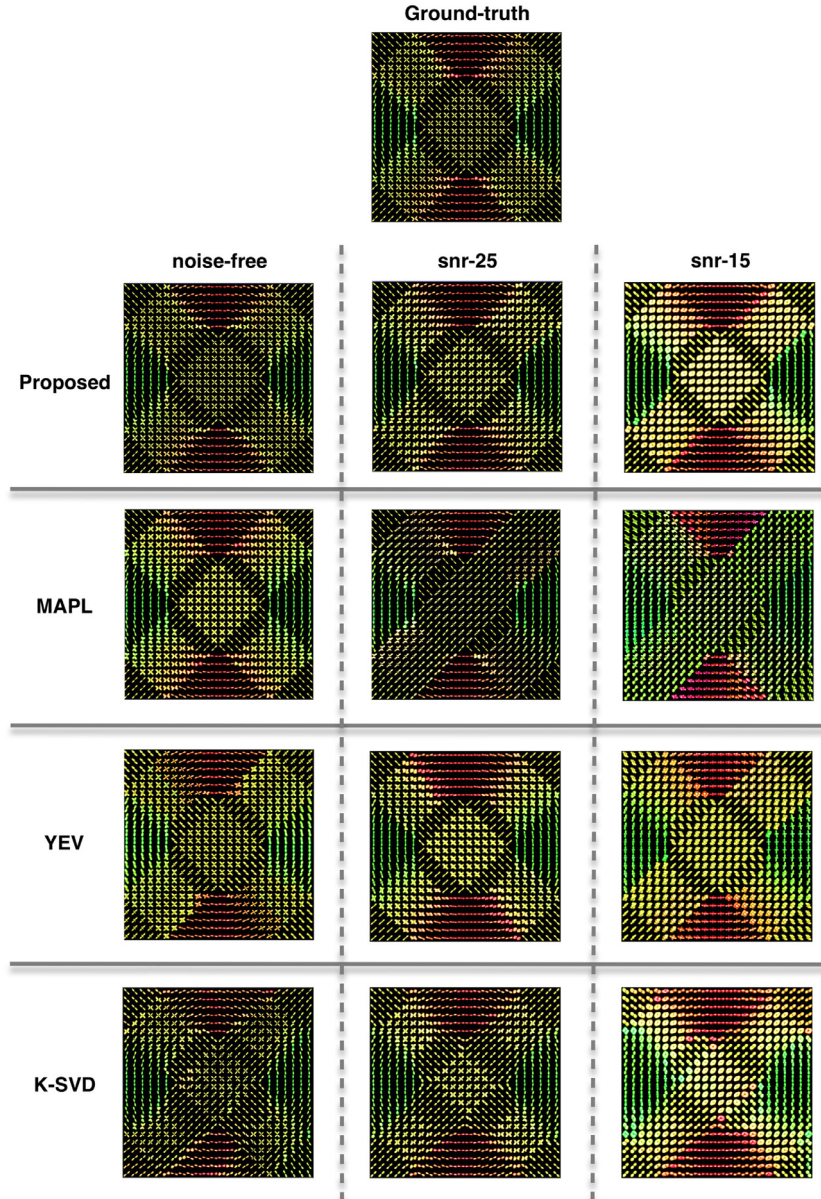


Fig. 4. Average angular errors in regions with crossing fibers estimated from EAP reconstructions using all the competing methods on noise-free and noisy synthetic data with various SNRs.



**Fig. 5.** Ground-truth EAP field (top row) and the EAP fields reconstructed from noise-free and noisy synthetic data (with an SNR of 25 and 15) using all the competing methods. Left to right depicts reconstructions for: noise-free, SNR = 25 and SNR = 15, respectively. Top to bottom depicts reconstructions using different approaches: proposed method, MAPL, YEV and K-SVD, respectively.

the impact of noise on the reconstructed EAPs. However, its angular discrimination power at the boundaries of the crossing regions deteriorates rapidly with added noise. This phenomenon can be observed in the bottom row of Fig. 6, where the K-SVD framework failed to recover the second peak at the margin of most crossing areas for data with SNR = 25. On the other hand, with MAPL, the presence of noise leads to underestimation of the propagator along one of the fiber orientations in the crossing regions (shown in Fig. 5). This can sometimes cause mis-detection of crossings, as can be seen in the case of SNR = 25 (in Fig. 6), where the number of peaks was estimated to be 1 in regions where crossings are present. It can also cause additional false peaks to emerge, as the estimated propagator value along the true fiber orientation is not prominent enough which causes other orientations with similar magnitude to be also detected as peaks, as in the case of SNR = 15. As to the method YEV, the reconstructed EAP fields appear to be of satisfactory quality for all data instances visually, but a large num-

ber of false peaks were detected from the EAP reconstructions obtained on data with a low SNR. This was not reflected in the numerical angular error results in Fig. 4 because the true fiber orientations are still dominant in the reconstructed EAP profiles, as can be seen from the corresponding sub-figure in Fig. 5.

To summarize, the proposed method was able to accurately reconstruct smooth EAP fields from diffusion data simulated with very complex geometric configurations even in the presence of noise. The angular discriminative power, peak recovery as well as crossing angle estimation demonstrated by our approach is superior to all competing methods.

#### 4.3. ISBI HARDI challenge 2013 phantom data

In this section, we showcase the evaluation of our method on the ISBI HARDI challenge 2013 phantom data. For this dataset, we compared our method with only MAPL and K-SVD, as the

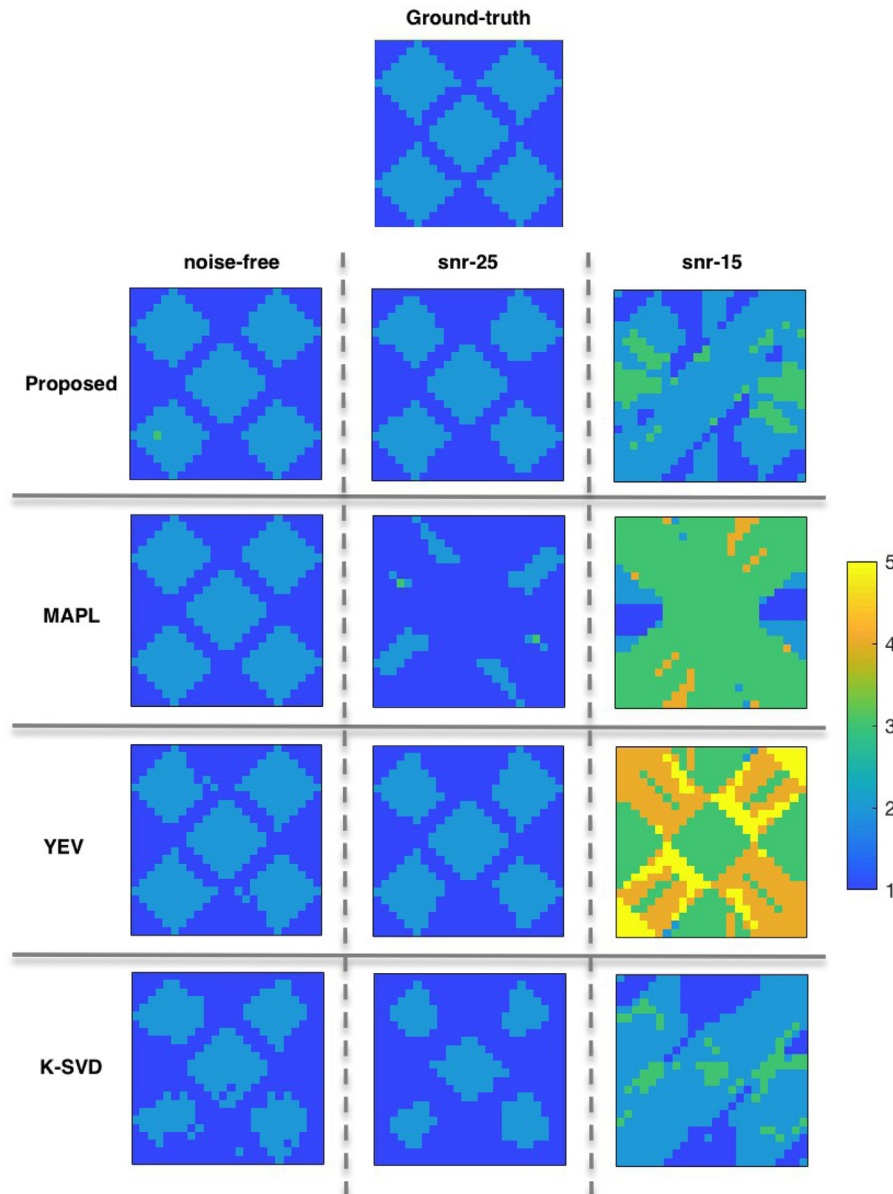


**Fig. 6.** Ground-truth number of EAP peaks (top row) and the number of peaks detected from EAP reconstructions using noise-free and noisy synthetic data (with an SNR of 25 and 15) using all the competing methods. Left to right depicts results from: noise-free, SNR = 25 and SNR = 15, respectively. Top to bottom depicts results from different approaches: proposed method, MAPL, YEV and K-SVD, respectively.

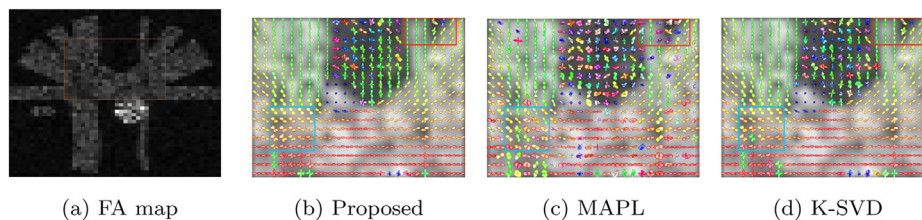


**Fig. 7.** EAP reconstructions for the ROI in the DSI phantom dataset with SNR = 10. (a) FA map of the slice, EAP reconstructions using (b) the proposed approach, (c) MAPL and (d) K-SVD.

approach, YEV, was not implemented for DSI acquisitions (Ye et al., 2012b). We selected our ROI within a slice where the various types of fiber configurations can be best observed, the FA map of which is presented in Fig. 7 for visualization purposes.

The EAP reconstructions from the 3 methods are presented in Fig. 7. As is evident from the figure, the proposed framework and K-SVD both produced coherent and smooth EAP fields while the

MAPL reconstructions suffered severely from the noise. In addition, crossing fibers were more accurately recovered by the two patch-based DL approaches (one example is shown in the blue rectangle highlighted region). This good performance can be attributed to the use of patch-based approaches in these two methods (which share the same pipeline/ framework presented in Section 2.5). Since the data generated with the highest noise level (SNR of 10)

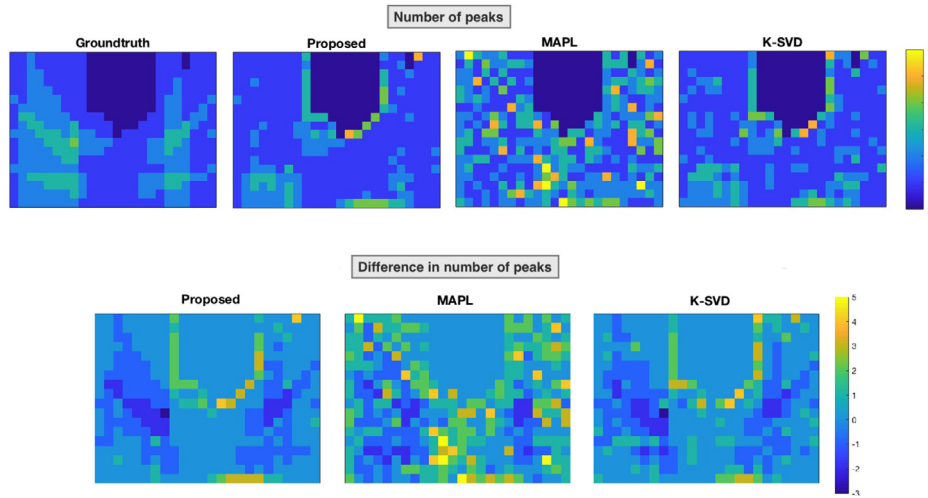


**Fig. 8.** Comparison of number of peaks for phantom data. Top row: ground-truth number of peaks (left) and the number of peaks detected from EAP reconstructions using the proposed method, MAPL and K-SVD (left to right). Bottom row: the difference of number of peaks between estimations using the 3 methods and the ground-truth. Note that different color (gray) -mapping schemes are used for the two rows, and the color (gray) -bars are presented separately.

was used in this experiment, as a result, the smoothing effect of the patch averaging operation played an important role in producing satisfactory results. Further, comparing the reconstructions from the proposed method and K-SVD, we noticed that in several regions where single fiber bundle passes through, spurious lobes exist in the EAP profiles reconstructed using the K-SVD approach (see the red rectangle enclosed region in Fig. 7).

As with synthetic data, for this dataset we also perform quantitative assessments on the EAP reconstructions. The estimated number of peaks remains a valuable metric in this evaluation. However, since the fiber configuration is far more complicated in the phantom, it is pointless and impossible to measure and compare crossing angles as we did for the synthetic data, in which the maximum number of fibers in an arbitrary voxel is 2. As an alternative, we look at the orientation of the peaks detected at every voxel and measure the difference between the estimated peak orientations and the ground-truth.

In Fig. 8, we present the ground-truth number of peaks in the ROI and the number of peaks detected in the EAP reconstructions from each method in the top row. Visually, the color (gray scale) field appears more smooth for the proposed method but it is to some degree difficult to determine between the proposed and the K-SVD results as to which of the two are of closer proximity to the ground-truth. Hence, we show in the second row the difference in the number of peaks with respect to the ground-truth for all the 3 methods. It is evident from these plots that the difference field from the proposed method has more voxels containing value 0 (represented by larger areas of the color teal), which indicates a better accuracy in the number of peaks detected. Moreover, the color (gray scale) field appears more regularized spatially for the proposed method compared to the competing ones.

The comparisons of angular error in fiber orientation estimates for the 3 methods are presented in Fig. 9. For every voxel, we measure the angle between each ground-truth fiber and the detected peak that forms the smallest angle with that fiber. The angular error for all ground-truth fibers are then averaged and mapped to a color (gray scale) and presented in the top row of Fig. 9 in a voxel-wise manner for each method. We also report the mean and the standard deviation of the error in the entire ROI within a text box for each method. The error field from our method presents great smoothness across the voxels and is visually darker (representing smaller values) overall compared to the fields produced by the competing methods. The histograms plotted below each color

(gray) field further verify that the angular error for fiber orientations estimated by the proposed approach are distributed closer to the y-axis. It is worth noting that for a dataset with an SNR as low as 10, our method is able to achieve highly accurate estimation of fiber orientations (within the range of the ground-truth orientation  $\pm 5$  degrees). This robustness to noise will be of immense value in practice for dMRI analysis.

#### 4.4. Wu-Minn HCP human brain data

A better understanding of brain connectivity and variability in healthy adults will yield profound insights into what contributes to the great variation in human behavioral capacities. It will lay the foundation for future studies of brain circuitry during development, aging and in various neurological disorders. The Human Connectome Project (HCP) strives towards this goal by collecting data using a wide variety of imaging modalities, including diffusion MR, functional MR etc., and sharing it together with rich behavioral and genetic information (Essen et al., 2013; Moeller et al., 2010; Feinberg et al., 2010; Setsompop et al., 2012; Xu et al., 2012; Glasser et al., 2013; Jenkinson et al., 2012; Fischl, 2012; Jenkinson et al., 2002). In HCP, diffusion imaging (HARDI, in particular) is used to chart the fiber trajectories and generate maps of structural connectivity in the brain via probabilistic tractography. In order to successfully apply probabilistic tractography, one needs rich information about the water diffusion process in the white matter, which can be succinctly provided by the EAPs reconstructed from the diffusion data.

In the following example, we show and discuss the EAP reconstruction results using the proposed method on a WU-Minn HCP dataset, to demonstrate its ability to capture information that can be used in characterizing the connectivity in the human brain. The acquisition details of this dataset were already presented in the previous section.

An area in centrum semiovale where projection, commissural and association tracts interact was picked as the ROI from a coronal slice, as highlighted in the FA map shown in Fig. 10(a). The EAPs reconstructed using all 4 methods are presented in the rest of the figure. As can be seen from the visual comparisons, the proposed method yields coherent and smooth reconstruction over the entire field, especially in regions of homogeneous fiber orientation such as the area enclosed by the orange ellipsoid. More importantly, the proposed method successfully recover crossings where

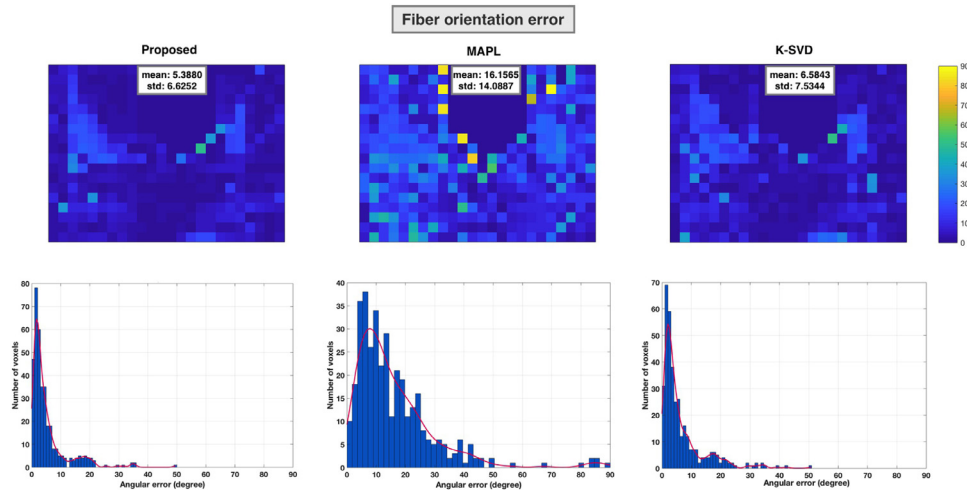


**Fig. 9.** Fiber orientation error comparisons for phantom data. Top row: error field of fiber orientations estimated from EAP reconstructions using the proposed method (left), MAPL (middle) and K-SVD (right), with the mean and standard deviation of the errors presented in a text box. Bottom row: the histogram and fitted distribution of the fiber orientation error for corresponding methods.

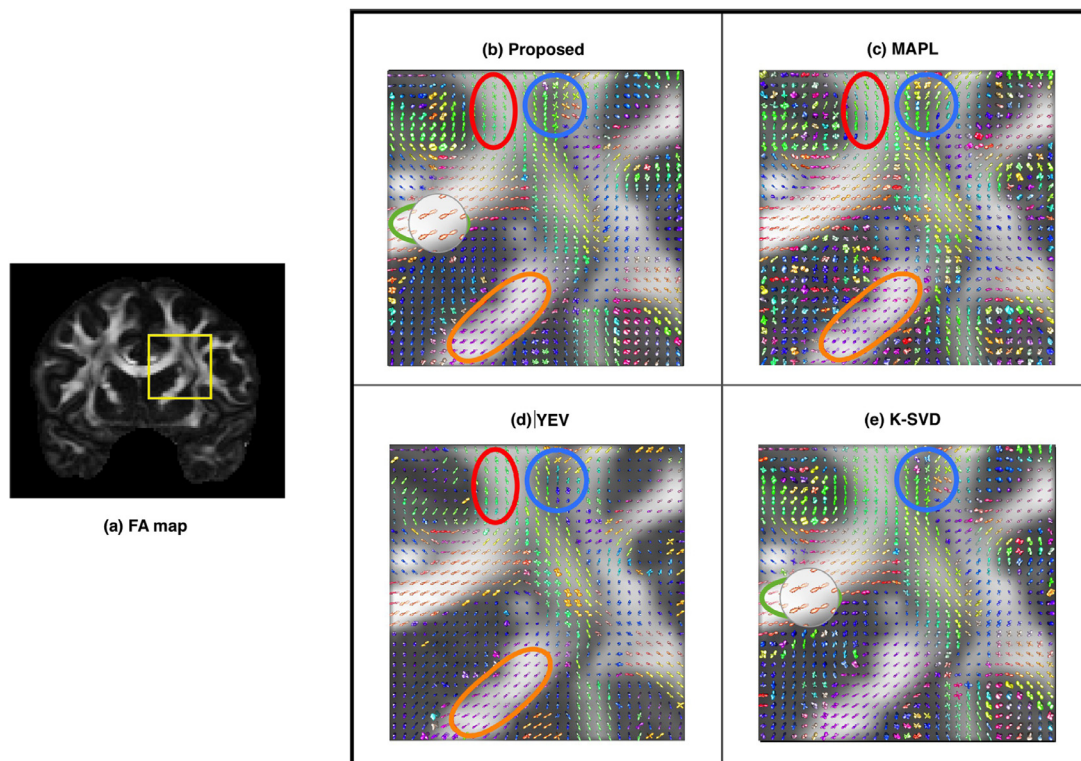


**Fig. 10.** EAP reconstruction from an ROI in a coronal slice of the HCP dataset. (a) FA map of the slice, EAP reconstructions using (b) the proposed method, (c) MAPL, (d) YEV and (e) K-SVD.

fiber tracts interact (see regions highlighted with red and blue circles). Comparing (b) and (e) we observed that the K-SVD framework performed relatively well on this dataset, which could be due to the advantage of employing a patch-based scheme in the framework. Another possible reason is that the EAP initialization (which was shared between the proposed and the K-SVD frameworks) was of great accuracy, which contributed to the high quality of the final results. Yet, in several regions it can be seen that spurious lobes were introduced in the K-SVD reconstruction, one example of this phenomena is highlighted in a green ellipsoid and zoomed in for closer inspection in the figure. Further, note that due to the assumption of a Euclidean vector space structure in K-SVD, the EAPs

reconstructed with the K-SVD do not necessarily satisfy the EAP non-negativity condition.

#### 4.5. Rat spinal cord injury data

In this section, we present another set of real data experiments involving HARDI acquisitions from control and injured rat spinal cords. We first present a brief biological motivation for this experiment and then present results of EAP reconstructions along with estimated HA maps and a statistical two sample *t*-test based validation.

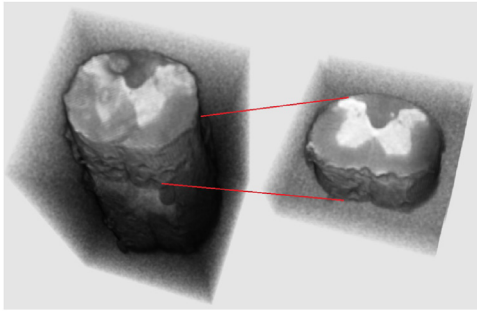


**Fig. 11.** 3D renderings of the spinal cord and the selected C4 section of a healthy rat.

Somatic and autonomic functions are profoundly disrupted by spinal cord injury (SCI), but some degree of spontaneous recovery is often possible following anatomically incomplete lesion. The relative extent of the functional recovery depends on multiple factors, the most prominent being the size and location of the spinal lesion. However, neuroplastic processes at sites distant to the primary site of spinal trauma are fundamentally important to the recovery process after SCI. For example, propriospinal neurons can effectively establish a “relay pathway” at sites many segments removed from the primary site of SCI, and these *de novo* pathways make a significant contribution to motor recovery after injury (Bareyre et al., 2004; Gerasimenko et al., 2007; Courtine et al., 2008; Harkema, 2008; Courtine et al., 2009). In addition, following SCI-induced axotomy, the relative extent of neurodegeneration at distant sites will have a considerable impact on the success of rehabilitation paradigms which target induction of spinal neuroplasticity. Thus, a deeper understanding of how SCI impacts the neuronal substrate proximal to lesion sites is important to optimizing motor recovery and future development of personalized rehabilitation paradigms directed more specifically at the available neurologic substrate.

For this purpose, we used HARDI acquisitions of spinal cords (C4 section) from 8 controls and 12 moderately injured rats, with 21 gradient directions at  $b$ -value  $1000 \text{ s/mm}^2$ . The rats in the moderately injured group received a contusion with 200 kdyn force applied to the T10 vertebral level of the spinal cord, which is distant to the imaging site (C4). In this experiment we are interested in testing the ability of the proposed method at producing high quality EAP reconstructions that can potentially assist the identification of neurodegeneration at sites distant to the spinal cord trauma. Fig. 11 provides examples of 3D renderings from the  $S_0$  image of the entire spinal cord as well as the C4 section from a control (spinal-intact) rat. The diffusion images of the C4 sections of all rats were co-registered prior to the EAP estimation. The HARDI acquisition parameters for this dataset have already been presented in the previous section.

We first randomly chose one rat from each of the two groups (injured and control rats) to showcase the results. For both rats, the cervical (C4) section (which is distant to the injury site T10) was evaluated using the EAP reconstruction framework developed herein and the results are presented. For this data set, we compare results from the proposed method only with the methods YEV and MAPL, due to the fact that the K-SVD method did not yield comparable result.

For a selected slice in the C4 region of the spinal cord, Fig. 12 shows the FA map for the control rat (top row) and injured rat (bottom row) overlaid with the reconstructed EAPs in this ROI using different methods. Comparing the results from different methods for a single rat (horizontally across in a figure), we can see that the proposed approach yields a coherent EAP field for both the rats, while some of the reconstructed EAP fields using compet-

ing methods are not as coherent. Further, the connectivities evident in the reconstructed EAP field using the proposed framework appear more plausible. We noticed that the fiber orientations recovered using different approaches do not completely agree (both in the case of healthy and injured rat). This is likely a result of the method MAPL and YEV being more suitable for data acquired at higher angular resolutions, while the data used here was acquired using only 21 gradient directions. On the other hand, comparing the reconstructed EAP field for the different rats using the same approach (vertically column-wise in the figure), it is evident that the distinction between the two rats produced by the proposed method is far more clear and significant.

**Imaging stain computation experiments:** The anisotropic index (HA) computed from the reconstructed EAP fields, for both the control and injured cords, are shown in Figs. 13 and 14, respectively. In all the experiments presented in this section,  $n = 724$  in Eq. (5). The images in the top rows of Figs. 13 and 14 were computed using an empirically determined  $\beta = 0.1$  (using a grid search). The visualization convention used here for an HA map depicts anisotropic regions to be brighter than isotropic regions.

Although, diffusion tensor model based biomarkers like fractional anisotropy (FA) etc. are still widely used clinical biomarker in practice, it is well known now that they can not cope with crossing fibers. In contrast, HA computed from any higher order tensors or other models of estimating EAPs overcomes this weaknesses. Besides, unlike many state-of-the-art biomarkers like RTAP, RTOP, RTPP (Özarslan et al., 2013; Fick et al., 2016), HA is not constrained to EAPs represented parameterically. Instead, computing HA from reconstructed EAP/ODF only requires one to evaluate Eqs. (5) and (6), which is straight-forward provided the EAPs/ODFs are probability distributions.

In Figs. 13 and 14, the comparison between HA maps obtained from the proposed method, MAPL and YEV, corroborates our previous claim that the proposed method produces more reliable coherent EAP reconstruction. Using our proposed method, with MAPL (isotropic) initialization, within ascending tracts more anisotropic regions have been detected in dorsal columns and spino-thalamic region, whereas within descending tracts, more anisotropic regions have been detected in reticulospinal region. On the other hand, using MAPL with the anisotropic setting, we found more anisotropic regions around the ventral corticospinal tract. This can already be observed in the HA map obtained from the proposed method. We can also see that even with the anisotropic setting in MAPL, the white matter and gray matter contrast is still poor and HA computed with the proposed method is more coherent and meaningful.

As mentioned before, the parameter  $\beta$  controls the contrast between the anisotropic and isotropic regions. To demonstrate this, in the bottom rows of Figs. 13 and 14, we present HA maps computed using various methods with parameter  $\beta = 0.15$ . From the figures it is evident that by varying  $\beta$  the imaging stain obtained using the proposed method is much more stable than the competing methods. With increasing contrast between white and gray matter, performances of MAPL and YEV deteriorate rapidly. So, in this work we not only introduced a novel EAP reconstruction technique but also discussed a flexible framework to compute a biomarker, which is sensitive to complex fiber geometries present in the imaged sample.

To further compare the competing methods' ability to distinguish between the two classes of imaged spinal cords, we performed the two sample  $t$ -test based on the computed HA maps. We want to assess whether the biomarker computed from the reconstructed EAPs can meaningfully identify the changes in water diffusion at voxels distant to spinal cord trauma. For this test a significance level of 0.10 was considered. In the top row of Fig. 15 we present the  $t$ -test results obtained from various methods. For a

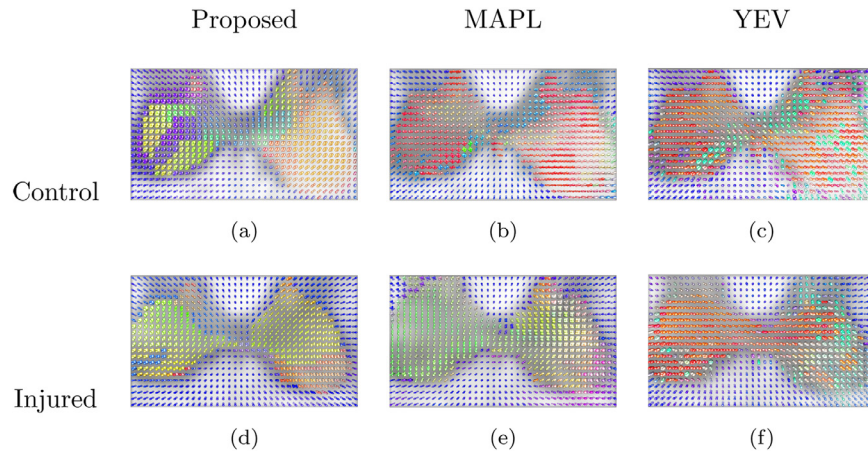


**Fig. 12.** EAP reconstruction for a selected slice in the C4 region of the spinal cord of a healthy rat (top row) and injured rat (bottom row). EAP reconstructions using the proposed method, MAPL and YEV, respectively.

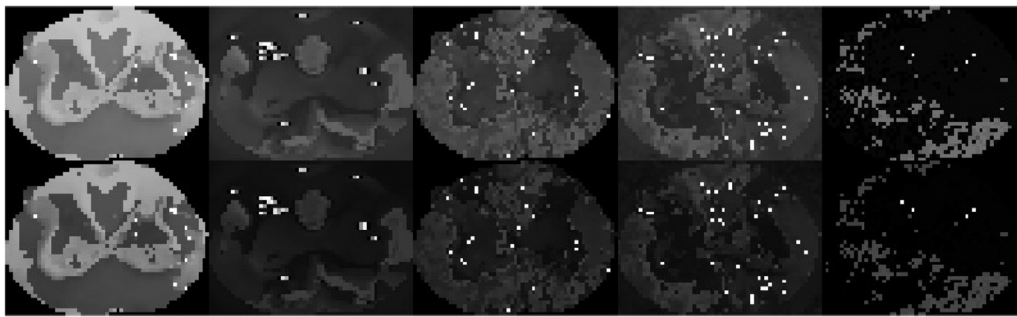


**Fig. 13.** HA maps for a selected slice in the C4 region of the spinal cord of a *control rat*. HA map with  $\beta = 0.10$  (top row) and  $\beta = 0.15$  (bottom row) computed from EAP reconstructions using (left to right) (1) the proposed method with YEV initialization, (2) the proposed method with MAPL (isotropic) initialization, (3) MAPL with isotropic setting, (4) MAPL with anisotropic setting and (5) YEV.

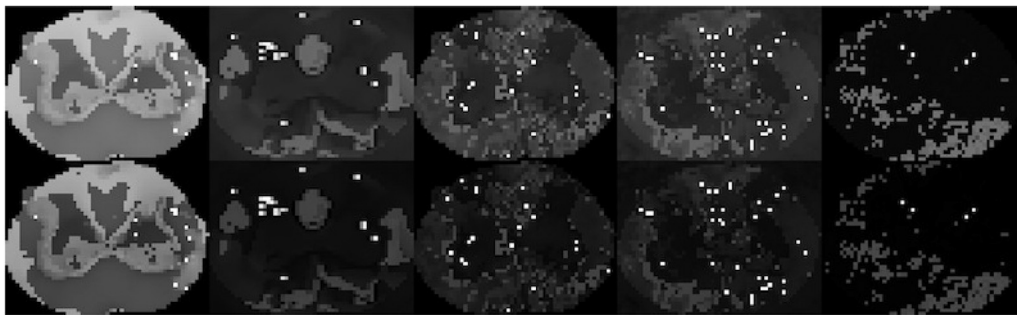


**Fig. 14.** HA maps for a selected slice in the C4 region of the spinal cord of an *injured rat*. HA map with  $\beta = 0.10$  (top row) and  $\beta = 0.15$  (bottom row) computed from EAP reconstructions using (left to right) (1) the proposed method with YEV initialization, (2) the proposed method with MAPL (isotropic) initialization, (3) MAPL with isotropic setting, (4) MAPL with anisotropic setting and (5) YEV.

better understanding, we superimposed the marked (red and green) significant voxels on a sample  $S_0$  image of the spinal cord (C4 section) of an injured rat. Both red and green regions are of significance. A green voxel indicates significantly increased anisotropy in the injured cord compared to a control, whereas a red voxel indicates a more isotropic diffusion in the injured cord. As observed earlier, the proposed method along with HA maps is far more adept at distinguishing between the two classes than MAPL and YEV. Though both YEV and MAPL failed to pick up the significant voxels in the ventral funiculus region, YEV was still able to identify some critical changes in the lateral edge of the spinal cord, but MAPL did not perform as well. Moreover, from the figures we can observe that the proposed method with MAPL initialization performed better than when initialized with YEV.

For better visualization, cross sectional images of the  $t$ -test results from various methods on a sample slice are presented in the bottom row of Fig. 15. In this figure, brightness (of the color) is *inversely proportional* to the p-value. From this result we can see that, all three methods were able to identify significant voxels in posterior median sulcus. For the injured rats, the proposed method and YEV also identified reduced anisotropy in the lateral spinal cord, which includes the region of the spinocerebellar tracts. But, both YEV and MAPL failed to identify the increased anisotropy of the injured cords in ventral funiculus region, where anterior spinothalamic and ventral corticospinal tracts are present. These results show that the proposed method is far more effective in capturing changes in neuroplasticity at sites distant to the primary site of spinal trauma, which is our primary goal in this example.

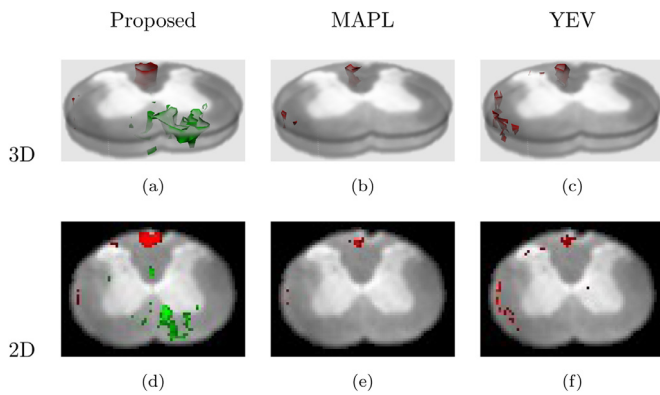


**Fig. 15.** (Top) T-test results in 3D with significance level 0.10 in C4 spinal region of the cord. Significant regions identified by (a) the proposed method, (b) MAPL and (c) YEV. (Bottom) A better visualization of the  $p$ -values via an arbitrarily selected slice in the C4 region.

The observed statistically significant increases and decreases in voxel anisotropy are likely to reflect a combination of neurodegeneration-induced decreases in fiber density coupled with sprouting and/or reorganization of propriospinal pathways. The literature has firmly established that the injured spinal cord undergoes profound neuroplastic remodeling (Bareyre et al., 2004; Fench and Rose, 2009; Filli and Schwab, 2015; Nakagawa et al., 2015), and the methods described herein may provide a tool to image these changes. For example, Fig. 15(a) indicates decreased voxel anisotropy in the dorsal column region (red shading), possibly indicating degeneration of propriospinal sensory afferent pathways (e.g., Type Ia, Ib). Fig. 15(a) also indicates increased anisotropy in the ventral-medial white matter, in the region of the spinoreticular and spinothalamic tracts, suggesting possible growth in these sensory pathways.

## 5. Discussion

Through a wide variety of experiments, we have demonstrated the superior performance of the proposed DL based EAP field reconstruction framework, with respect to accuracy in peak recovery, angular estimation as well as spatial coherence in the reconstruction. The comparisons with linear DL based EAP reconstruction methods clearly show the advantage of respecting and incorporating the manifold structure of EAPs. Further, the comparison with the state-of-the-art EAP/ODF reconstruction technique, MAPL, suffices to demonstrate the value of our approach relative to existing methods in the field.

The strengths of the proposed method are three-fold. First and foremost, it produces very accurate and spatially smooth reconstructions of EAP fields while providing guarantees for the non-negativity of the reconstructed EAPs in the presence of noise. Secondly, the dictionary learned in the reconstruction process is fully adaptive and tailored to the particular data at hand, with no assumptions on the model for signal or EAP representation. Last but not least, the framework presented herein is applicable to data acquired with any sampling scheme and maintains consistent performance, as demonstrated in the experiments. This independence with respect to the sampling scheme stems from the unique design of the pipeline, in which the EAPs are first initialized using any method of choice before being passed on to the DL algorithm. This design, meanwhile, makes the performance of the proposed approach dependent on the quality of the initialization to some extent. As in any method involving hard nonlinear optimization which depend on a good initial guess, our method is also dependent on the initialization. In our experiments, we found that our method initialized with YEV lead to more coherent output

compared to initialization with MAPL. However MAPL initialization yielded faster convergence despite the results being less coherent in comparison. Further theoretical analysis is however necessary to quantify the capture range of the method in terms of initializations for convergence and accuracy. This will involve significant mathematical analysis and is a possible venue of investigation for future work.

One of the key features of our method is that it is a patch-based Dictionary Learning method. Patch-based dictionary learning is well studied in the context of image denoising, inpainting, super-resolution, etc. Our patch-based algorithm is inspired by the success achieved in the task of image reconstruction in compressed sensed MRI by patch-based linear dictionaries reported in Ravishankar and Yoram (2011). The effect of size of patches on the quality of reconstruction is similar to that in any patch-based algorithms employed in image processing. Larger the patch size, smoother is the reconstruction at the expense of computational cost. Patch-size is similar to the scale parameter in scale-space methods and dictates the scale of reconstruction. Finer the desired scale of reconstruction, smaller the patch size. In our work, patch-size was determined via a grid search.

One of the limitations of the proposed framework is the higher computation time incurred in the non-linear DL process, typically ranging over thirty minutes to several hours. This computation time is dependent several factors namely, quality of the initialization and patch size (discussed above). Closer the initialization to the local optimum, faster will be the convergence. With regards to current limitation of the method in computation time, one possible venue to explore is to implement the entire pipeline in C and use GPU accelerated computations. We will explore this venue in our future work.

In this work, we proposed an effective biomarker based on Rényi entropy. This biomarker summarizes the diffusional characteristics captured by the reconstructed EAP. As EAPs are probability densities, this Rényi entropy based index is natural and easy to compute and unlike FA, it can also reflect anisotropy in the regions of crossing fibers. It is also not biased toward any chosen basis for EAP representations. Using a two sample  $t$ -test, we showed that the proposed biomarker can meaningfully capture significant structural changes between the control and injured cord groups distant from the site of injury.

## 6. Conclusions

In this paper, we presented a novel patch-based EAP field reconstruction technique from dMRI data sets. EAPs capture the diffusional characteristics of the tissue micro-architecture and hence are of fundamental importance to the inference of the structural changes. In the recent past, EAP field reconstruction has been commonly achieved via known basis expansions as well as dictionary learning and sparse coding based methods formulated in vector spaces. Here, we presented a generalization of the dictionary learning and sparse coding problem in Euclidean space to smooth (Riemannian) manifolds and discussed a two stage alternating minimization solver for this generalization. We applied this formulation to the EAP field reconstruction problem where the EAP field in a patch is represented as a point on the product manifold of square root densities. Using this patch-based approach, we achieved a smooth EAP field reconstruction from dMRI data. Through multiple synthetic, phantom and real data experiments, we demonstrated that our method outperforms vector-space dictionary learning based methods as well the state-of-the-art in EAP reconstruction namely, the MAPL method. This performance can be attributed to the incorporation of the geometric structure of the data space into the dictionary learning process in combination with the patch-based framework. Further, we also presented

an imaging stain/ biomarker (HA) that is a function of the well known Rényi entropy from information theory literature which has been widely employed in a variety of applications. This biomarker is easy to compute from the estimated EAPs, is unbiased to the choice of EAP representations and is an effective tool in capturing complex diffusion patterns in the tissue being imaged. Using a two-sample *t*-test, we presented quantitative results depicting the ability of the imaging biomarker (HA) to capture changes in the tissue microstructure of the spinal cord distant from the site of the injury.

### Conflict of interest

We wish to draw the attention of the Editor to the following facts which may be considered as potential conflicts of interest and to significant financial contributions to this work. [OR] We wish to confirm that there are no known conflicts of interest associated with this publication and there has been no significant financial support for this work that could have influenced its outcome.

We confirm that the manuscript has been read and approved by all named authors and that there are no other persons who satisfied the criteria for authorship but are not listed. We further confirm that the order of authors listed in the manuscript has been approved by all of us.

We confirm that we have given due consideration to the protection of intellectual property associated with this work and that there are no impediments to publication, including the timing of publication, with respect to intellectual property. In so doing we confirm that we have followed the regulations of our institutions concerning intellectual property.

### Acknowledgment

The authors gratefully acknowledge Yuchen Xie, Wenxing Ye and Jeffrey Ho for their contributions at the beginning of this project. This research was in part funded by the NSF grants IIS 1525431 and IIS 1724174 to Baba C. Vemuri, and the ONR grant N00014-14-1-0762 and NSF grant IIS-1617101 to Alireza Entezari.

Data were provided in part by the Human Connectome Project, WU-Minn Consortium (Principal Investigators: David Van Essen and Kamil Ugurbil; 1U54MH091657) funded by the 16 NIH Institutes and Centers that support the NIH Blueprint for Neuroscience Research; and by the McDonnell Center for Systems Neuroscience at Washington University.

### References

- Absil, P.-A., Mahony, R.E., Sepulchre, R., 2008. *Optimization Algorithms on Matrix Manifolds*. Princeton University Press.
- Afsari, B., 2011. Riemannian  $L^p$  center of mass: existence, uniqueness, and convexity. *Proc. Am. Math. Soc.* 139 (2), 655–673.
- Aharon, M., Elad, M., Bruckstein, A., 2006. K-SVD: an algorithm for designing over-complete dictionaries for sparse representation. *IEEE Trans. Signal Process.* 54 (11), 4311–4322.
- Aranda, R., Ramirez-Manzanares, A., Rivera, M., 2015. Sparse and adaptive diffusion dictionary (SADD) for recovering intra-voxel white matter structure. *Med. Image Anal.* 26 (1), 243–255. doi:10.1016/j.media.2015.10.002.
- Assemal, H., Tschumperlé, D., Brun, L., 2009. Efficient and robust computation of PDF features from diffusion MR signal. *Med. Image Anal.* 13 (5), 715–729. doi:10.1016/j.media.2009.06.004.
- Assemal, H.-E., Tschumperlé, D., Brun, L., Siddiqi, K., 2011. Recent advances in diffusion MRI modeling: angular and radial reconstruction. *Med. Image Anal.* 15 (4), 369–396.
- Bareyre, F.M., Kerschensteiner, M., Raineteau, O., Mettenleiter, T.C., Weinmann, O., Schwab, M.E., 2004. The injured spinal cord spontaneously forms a new intraspinal circuit in adult rats. *Nat. Neurosci.* 7 (3), 269–277.
- Basser, P., Mattiello, J., Lebihan, D., 1994. Estimation of the effective self-diffusion tensor from the NMR spin echo. *J. Magn. Reson. B* 3103 (3), 247–254.
- Bilgic, B., Chatnuntawech, I., Setsompop, K., Cauley, S.F., Yendiki, A., Wald, L.L., Adalsteinsson, E., 2013. Fast dictionary-based reconstruction for diffusion spectrum imaging. *IEEE Trans. Med. Imaging* 32 (11), 2022–2033.
- Callaghan, P.T., 1991. *Principles of Nuclear Magnetic Resonance Microscopy*. Oxford University Press.
- Çetingül, H.E., Vidal, R., 2011. Sparse Riemannian manifold clustering for HARDI segmentation. In: *Proceedings of the IEEE International Symposium on Biomedical Imaging, ISBI*, pp. 1750–1753.
- Cheng, J., Ghosh, A., Jiang, T., Deriche, R., 2010. Model-free and analytical EAP reconstruction via spherical polar Fourier diffusion MRI. In: *Proceedings of the Medical Image Computing and Computer-Assisted Intervention–MICCAI*. Springer, Berlin/Heidelberg, pp. 590–597.
- Cheng, J., Jiang, T., Deriche, R., 2012. Nonnegative definite EAP and ODF estimation via a unified multi-shell HARDI reconstruction. In: *Proceedings of the Medical Image Computing and Computer-Assisted Intervention–MICCAI Part II*, pp. 313–321.
- Cheng, J., Jiang, T., Deriche, R., Shen, D., Yap, P., 2013. Regularized spherical polar Fourier diffusion MRI with optimal dictionary learning. In: *Proceedings of the Medical Image Computing and Computer-Assisted Intervention–MICCAI, Part I*, pp. 639–646. doi:10.1007/978-3-642-40811-3\_80.
- Cheng, J., Shen, D., Yap, P.-T., Basser, P.J., 2015. Tensorial spherical polar Fourier diffusion MRI with optimal dictionary learning. In: *Proceedings of the International Conference on Medical Image Computing and Computer-Assisted Intervention*. Springer, pp. 174–182.
- Cherian, A., Sra, S., 2014. Riemannian sparse coding for positive definite matrices. In: *Proceedings of the European Conference on Computer Vision–ECCV, Part III*, pp. 299–314. doi:10.1007/978-3-319-10578-9\_20.
- Cook, P., Bai, Y., Nedjati-Gilani, S., Seunarine, K., Hall, M., Parker, G., Alexander, D., 2006. Camino: open-source diffusion-MRI reconstruction and processing. In: *Proceedings of the Fourteenth Scientific Meeting of the International Society for Magnetic Resonance in Medicine*, 2759. Seattle WA, USA.
- Courtine, G., Gerasimenko, Y., Van Den Brand, R., Yew, A., Musienko, P., Zhong, H., Song, B., Ao, Y., Ichiyama, R.M., Lavrov, I., et al., 2009. Transformation of non-functional spinal circuits into functional states after the loss of brain input. *Nat. Neurosci.* 12 (10), 1333–1342.
- Courtine, G., Song, B., Roy, R.R., Zhong, H., Herrmann, J.E., Ao, Y., Qi, J., Edgerton, V.R., Sofroniew, M.V., 2008. Recovery of supraspinal control of stepping via indirect propriospinal relay connections after spinal cord injury. *Nat. Med.* 14 (1), 69–74.
- Daducci, A., Canales-Rodríguez, E.J., Descoteaux, M., Garyfallidis, E., Gur, Y., Lin, Y.-C., Mani, M., Merlet, S., Paquette, M., Ramirez-Manzanares, A., et al., 2014. Quantitative comparison of reconstruction methods for intra-voxel fiber recovery from diffusion MRI. *IEEE Trans. Med. Imaging* 33 (2), 384–399.
- Daducci, A., Caruyer, E., Descoteaux, M., Thiran, J., 2013. HARDI reconstruction challenge. In: *Proceedings of the IEEE International Symposium on Biomedical Imaging*. <http://hardi.epfl.ch/statistics/>.
- Descoteaux, M., Deriche, R., Le Bihan, D., Mangin, J.-F., Poupon, C., 2009. Diffusion propagator imaging: using Laplace equation and multiple shell acquisitions to reconstruct the diffusion propagator. In: *Proceedings of the International Conference on Information Processing in Medical Imaging*. Springer, pp. 1–13.
- Descoteaux, M., Deriche, R., Le Bihan, D., Mangin, J.-F., Poupon, C., 2011. Multiple q-shell diffusion propagator imaging. *Med. Image Anal.* 15 (4), 603–621.
- Elad, M., 2010. *Sparse and Redundant Representations - From Theory to Applications in Signal and Image Processing*. Springer doi:10.1007/978-1-4419-7011-4.
- Essen, D.C.V., Smith, S.M., Barch, D.M., Behrens, T.E.J., Yacoub, E., Ugurbil, K., 2013. The WU-Minn human connectome project: an overview. *NeuroImage* 80, 62–79.
- Feinberg, D.A., Moeller, S., Smith, S.M., Auerbach, E., Ramanna, S., Glasser, M.F., Miller, K.L., Ugurbil, K., Yacoub, E., 2010. Multiplexed echo planar imaging for sub-second whole brain fMRI and fast diffusion imaging. *PLoS One* 5 (12), e15710.
- Fenrich, K.K., Rose, P.K., 2009. Spinal interneuron axons spontaneously regenerate after spinal cord injury in the adult feline. *J. Neurosci.* 29 (39), 12145–12158.
- Feragen, A., Lauze, F., Hauberg, S., 2015. Geodesic exponential kernels: when curvature and linearity conflict. In: *Proceedings of the IEEE Conference on Computer Vision and Pattern Recognition, CVPR*, pp. 3032–3042. doi:10.1109/CVPR.2015.7298922.
- Fick, R.H., Wassermann, D., Caruyer, E., Deriche, R., 2016. MAPL: tissue microstructure estimation using Laplacian-regularized MAP-MRI and its application to HCP data. *NeuroImage* 134, 365–385.
- Filli, L., Schwab, M.E., 2015. Structural and functional reorganization of propriospinal connections promotes functional recovery after spinal cord injury. *Neural Regen. Res.* 10 (4), 509.
- Fischl, B., 2012. Freesurfer. *NeuroImage* 62 (2), 774–781.
- Fletcher, P.T., Joshi, S.C., 2007. Riemannian geometry for the statistical analysis of diffusion tensor data. *Signal Process.* 87 (2), 250–262.
- Garyfallidis, E., Brett, M., Amirbekian, B., Rokem, A., Van Der Walt, S., Descoteaux, M., Nimmo-Smith, I., Contributors, D., 2014. Dipy, a library for the analysis of diffusion MRI data. *Front. Neuroinform.* 8. doi:10.3389/fninf.2014.00008.
- Gerasimenko, Y.P., Ichiyama, R.M., Lavrov, I.A., Courtine, G., Cai, L., Zhong, H., Roy, R.R., Edgerton, V.R., 2007. Epidural spinal cord stimulation plus quipazine administration enable stepping in complete spinal adult rats. *J. Neurophysiol.* 98 (5), 2525–2536.
- Glasser, M.F., Sotiropoulos, S.N., Wilson, J.A., Coalson, T.S., Fischl, B., Andersson, J.L., Xu, J., Jbabdi, S., Webster, M., Polimeni, J.R., et al., 2013. The minimal preprocessing pipelines for the human connectome project. *NeuroImage* 80, 105–124.
- Harandi, M.T., Salzmann, M., 2015. Riemannian coding and dictionary learning: kernels to the rescue. In: *Proceedings of the IEEE Conference on Computer Vision and Pattern Recognition, CVPR*, pp. 3926–3935. doi:10.1109/CVPR.2015.7299018.
- Harkema, S.J., 2008. Plasticity of interneuronal networks of the functionally isolated human spinal cord. *Brain Res. Rev.* 57 (1), 255–264.

- Jenkinson, M., Bannister, P., Brady, M., Smith, S., 2002. Improved optimization for the robust and accurate linear registration and motion correction of brain images. *NeuroImage* 17 (2), 825–841.
- Jenkinson, M., Beckmann, C.F., Behrens, T.E.J., Woolrich, M.W., Smith, S.M., 2012. FSL. *NeuroImage* 62 (2), 782–790.
- Jian, B., Vemuri, B.C., Özarslan, E., Carney, P.R., Mareci, T.H., 2007. A novel tensor distribution model for the diffusion-weighted MR signal. *NeuroImage* 37, 164–176.
- Lane, M.A., Lee, K.-Z., Salazar, K., O'Steen, B.E., Bloom, D.C., Fuller, D.D., Reier, P.J., 2012. Respiratory function following bilateral mid-cervical contusion injury in the adult rat. *Exp. Neurol.* 235 (1), 197–210.
- Lee, J.M., 1997. Riemannian manifold: an introduction to curvature. Springer-Verlag, New York, NY.
- Leglet, C., Rousson, M., Deriche, R., 2006. DTI segmentation by statistical surface evolution. *IEEE Trans. Med. Imaging* 25 (6), 685–700.
- Mcgraw, T.E., Vemuri, B.C., 2005. Denoising, segmentation and visualization of diffusion weighted MRI. University of Florida Ph.D. thesis.
- Merlet, S., Caruyer, E., Ghosh, A., Deriche, R., 2013. A computational diffusion MRI and parametric dictionary learning framework for modeling the diffusion signal and its features. *Med. Image Anal.* 17 (7), 830–843. doi:10.1016/j.media.2013.04.011.
- Merlet, S.L., Deriche, R., 2013. Continuous diffusion signal, EAP and ODF estimation via compressive sensing in diffusion MRI. *Med. Image Anal.* 17 (5), 556–572.
- Michailovich, O., Rathi, Y., 2010. On approximation of orientation distributions by means of spherical ridgelets. *IEEE Trans. Image Process.* 19 (2), 461–477.
- Moakher, M., 2005. A differential geometric approach to the geometric mean of symmetric positive-definite matrices. *SIAM J. Matrix Anal. Appl.* 26 (3), 735–747.
- Moeller, S., Yacoub, E., Olman, C.A., Auerbach, E., Strupp, J., Harel, N., Ugurbil, K., 2010. Multiband multislice GE-EPI at 7 tesla, with 16-fold acceleration using partial parallel imaging with application to high spatial and temporal whole-brain fMRI. *Magn. Reson. Med.* 63 (5), 1144–1153.
- Nakagawa, H., Ninomiya, T., Yamashita, T., Takada, M., 2015. Reorganization of corticospinal tract fibers after spinal cord injury in adult macaques. *Sci. Rep.* 5, 11986.
- Ncube, S., Srivastava, A., 2011. A novel Riemannian metric for analyzing HARDI data. In: *Proceedings of the SPIE*, 7962.
- Özarslan, E., Koay, C., Basser, P., 2008. Simple harmonic oscillator based estimation and reconstruction for one-dimensional q-space mr. In: *Proceedings of the International Society for Magnetic Resonance in Medicine (ISMRM)*, 16, p. 35.
- Özarslan, E., Koay, C.G., Shepherd, T.M., Komlosh, M.E., İrfanoğlu, M.O., Pierpaoli, C., Basser, P.J., 2013. Mean apparent propagator (MAP) MRI: a novel diffusion imaging method for mapping tissue microstructure. *NeuroImage* 78, 16–32.
- Özarslan, E., Shepherd, T.M., Vemuri, B.C., Blackband, S.J., Mareci, T.H., 2006. Resolution of complex tissue microarchitecture using the diffusion orientation transform (DOT). *NeuroImage* 31, 1086–1103.
- Panagiotaki, E., Schneider, T., Siow, B., Hall, M.G., Lythgoe, M.F., Alexander, D.C., 2012. Compartment models of the diffusion MR signal in brain white matter: a taxonomy and comparison. *NeuroImage* 59 (3), 2241–2254.
- Penec, X., Fillard, P., Ayache, N., 2006. A Riemannian framework for tensor computing. *Int. J. Comput. Vis.* 66 (1), 41–66.
- Rathi, Y., Michailovich, O., Laun, F., Setsompop, K., Grant, P.E., Westin, C.-F., 2014. Multi-shell diffusion signal recovery from sparse measurements. *Med. Image Anal.* 18 (7), 1143–1156.
- Ravishanker, S., Yoram, B., 2011. Mr image reconstruction from highly undersampled k-space data by dictionary learning. *IEEE Trans. Med. Imaging* 30 (5), 1028–1041.
- Rényi, A., 1961. On measures of entropy and information. Technical Report. Hungarian Academy of Sciences, Budapest, Hungary.
- Schwab, E., Afsari, B., Vidal, R., 2012. Estimation of non-negative ODFs using the eigenvalue distribution of spherical functions. In: *Proceedings of the Medical Image Computing and Computer-Assisted Intervention–MICCAI, Part II*, pp. 322–330.
- Schwab, E., Vidal, R., Charon, N., 2016. Spatial-angular sparse coding for HARDI. In: *Proceedings of the International Conference on Medical Image Computing and Computer-Assisted Intervention (MICCAI)*. Springer International Publishing, pp. 475–483.
- Setsompop, K., Gagoski, B.A., Polimeni, J.R., Witzel, T., Wedeen, V.J., Wald, L.L., 2012. Blipped-controlled aliasing in parallel imaging for simultaneous multislice echo planar imaging with reduced g-factor penalty. *Magn. Reson. Med.* 67 (5), 1210–1224.
- Sivalingam, R., Boley, D., Morellas, V., Papanikolopoulos, N., 2015. Tensor dictionary learning for positive definite matrices. *IEEE Trans. Image Process.* 24 (11), 4592–4601. doi:10.1109/TIP.2015.2440766.
- Song, Y., Zhu, Z., Lu, Y., Liu, Q., Zhao, J., 2014. Reconstruction of magnetic resonance imaging by three-dimensional dual-dictionary learning. *Magn. Reson. Med.* 71, 1285–1298.
- Spivak, M., 1979. *A Comprehensive Introduction to Differential Geometry, One, Third ed.* Publish or Perish, Inc., Houston, Texas.
- Sun, J., Qu, Q., Wright, J., 2015. Complete dictionary recovery over the sphere. *CoRR* abs/1504.06785.
- Sun, J., Xie, Y., Ye, W., Ho, J., Entezari, A., Blackband, S.J., Vemuri, B.C., 2013. Dictionary learning on the manifold of square root densities and application to reconstruction of diffusion propagator fields. In: *Proceedings of the Twenty third International Conference on Information Processing in Medical Imaging IPMI*, pp. 619–631. doi:10.1007/978-3-642-38868-2\_52.
- Wang, Z., Vemuri, B.C., 2005. DTI segmentation using an information theoretic tensor dissimilarity measure. *IEEE Trans. Med. Imaging* 24 (10), 1267–1277.
- Wedeen, V.J., Hagmann, P., Tseng, W.Y., Reese, T.G., Weisskoff, R.M., 2005. Mapping complex tissue architecture with diffusion spectrum magnetic resonance imaging. *Magn. Reson. Med.* 54 (6), 1377–1386.
- Wu, Y., Jia, Y., Li, P., Zhang, J., Yuan, J., 2015. Manifold kernel sparse representation of symmetric positive-definite matrices and its applications. *IEEE Trans. Image Process.* 24 (11), 3729–3741. doi:10.1109/TIP.2015.2451953.
- Xie, Y., Vemuri, B.C., Ho, J., 2010. Statistical analysis of tensor fields. In: *Proceedings of the Medical Image Computing and Computer-Assisted Intervention–MICCAI, Part I*, pp. 682–689.
- Xu, J., Moeller, S., Strupp, J., Auerbach, E., Chen, L., Feinberg, D., Ugurbil, K., Yacoub, E., 2012. Highly accelerated whole brain imaging using aligned-blipped-controlled-aliasing multiband EPI. In: *Proceedings of the Twentieth Annual Meeting of ISMRM*, 2306.
- Ye, C., Zhuo, J., Gullapalli, R.P., Prince, J.L., 2016. Estimation of fiber orientations using neighborhood information. *Med. Image Anal.* 32, 243–256.
- Ye, W., Portnoy, S., Entezari, A., Blackband, S.J., Vemuri, B.C., 2012. An efficient inter-leaved multi-shell sampling scheme for reconstruction of diffusion propagators. *IEEE Trans. Med. Imaging* 31 (5), 1043–1050.
- Ye, W., Vemuri, B.C., Entezari, A., 2012. An over-complete dictionary based regularized reconstruction of a field of ensemble average propagators. In: *Proceedings of the IEEE International Symposium on Biomedical Imaging, ISBI*, pp. 940–943.
- Yoldemir, B., Bajammal, M., Abugharbieh, R., 2014. Dictionary based super-resolution for diffusion MRI. In: *Computational Diffusion MRI*, pp. 203–213.